Investigation of 3D-effects for UV / vis satellite and ground based observations of volcanic plumes

5 Thomas Wagner[1], Simon Warnach[1,2], Steffen Beirle[1], Nicole Bobrowski[2,3], Adrian Jost[1], Janis Puķīte[1], and Nicolas Theys[4]

[1]Satellite Remote Sensing Group, Max Planck Institute for Chemistry, Mainz, Germany
[2]Institute of Environmental Physics, University of Heidelberg, Heidelberg, Germany
[3]Istituto Nazionale Geofisica e Vulcanologia Catania, Italy
10 [4]Royal Belgian Institute for Space Aeronomy (BIRA-IASB), Brussels, Belgium

Correspondence to: Thomas Wagner (thomas.wagner@mpic.de)

Abstract. We investigate effects of the 3-dimensional (3D) structure of volcanic plumes on the retrieval results of satellite and ground based UV-vis observations. For the analysis of such measurements usually 1D scenarios are assumed (the atmospheric properties only depend on altitude). While 1D assumptions are well suited for the analysis of many atmospheric 15 phenomena, they are usually less appropriate for narrow trace gas plumes. For UV/vis satellite instruments with large ground pixel sizes like GOME-2, SCIAMACHY, or OMI, 3D effects are of minor importance, but usually these observations are not sensitive to small volcanic plumes. In contrast, observations of TROPOMI aboard Sentinel-5P have a much smaller ground pixel size (3.5 x 5.5 km²). Thus on the one hand, TROPOMI can detect much smaller plumes than previous instruments. On 20 the other hand 3D effects become more important, because the TROPOMI ground pixel size is smaller than the height of the troposphere and also smaller than horizontal atmospheric photon path lengths in the UV/vis spectral range.

In this study we investigate the following 3D-effects using Monte-Carlo radiative transfer simulations: 1. the light mixing effect caused by horizontal photon paths, 2. the saturation effect for strong SO_2 absorption, 3. geometric effects related to slant illumination and viewing angles, and 4. Plume side effects related to slant illumination angles and photons reaching the 25 sensor from the sides of volcanic plumes. Especially the first two effects can lead to a strong and systematic underestimation if 1D retrievals are applied (more than 50% for the light mixing effect, and up to 100% for the saturation effect). Besides the atmospheric radiative transfer, the saturation effect also affects the the spectral retrievals. Geometric effects have a weaker influence on the quantitative analyses, but can lead to a spatial smearing of elevated plumes or even to virtual double plumes. Plume side effects are small for short wavelengths, but can become large for longer wavelengths (up to 100% for slant 30 viewing and illumination angles). For ground based observations, most of the above mentioned 3D effects are not important, because of the narrow FOV and the closer distance between the instrument and the volcanic plume. However, the light mixing effect shows a similar strong dependence on the horizontal plume extension as for satellite observations and should be taken into account for the analysis of ground based observations.

35 1 Introduction

SO_2 emitted from volcanoes is observed from satellites since about 40 years. After successful first detections for large eruptions by the TOMS instrument (Krueger, 1983), subsequent UV/vis satellite instruments with continuous spectral coverage allowed also the observation of smaller plume amounts (Eisinger and Burrows, 1998; Afe et al., 2004, Khokhar et 40 al., 2005, Krotkov et al., 2006; Yang et al., 2007, 2010; Nowlan et al., 2011; Rix et al., 2012; Hörmann et al., 2013; Li et al., 2013; Penning de Vries et al., 2014; Theys et al., 2015, Fioletov et al., 2016; Zhang et al., 2017; Theys et al., 2017, 2019, 2021a). Furthermore, besides SO_2, also other trace gases like BrO, OClO and IO in volcanic plumes could be analysed from these observations (Theys et al., 2009; Heue et al., 2011; Rix et al., 2012; Hörmann et al., 2013; Theys et al., 2014; Schönhardt et al., 2017; Suleiman et al., 2019).

Atmospheric
Measurement
Techniques
Discussions

45   Since the launch of the GOME-1 instrument aboard ERS-2 in 1995 (Burrows et al., 1999), the ground pixel size of UV/vis
      sensors has strongly decreased from 40 x 320 km² (GOME-1) down to 3.5 x 5.5 km² (TROPOMI), see Table 1. The ground
      pixel size of TROPOMI is thus only slightly larger or even similar to the extension of pollution plumes, in particular to those
      from small/medium volcanic eruptions or passive degassing. Thus with TROPOMI, many small/medium volcanic plumes
      become detectable, which could not be detected with the former instruments (also the high signal to noise ratio of TROPOMI

50   contributes to the increased sensitivity to small volcanic plumes). An example of TROPOMI observations of SO_2 and BrO
      for a narrow volcanic plume is shown in Fig. 1 (Warnach, 2022). Shown are the slant column densities (SCD, commonly
      interpreted as the integrated concentrations along the light path) of both trace gases.

      To illustrate the effects of this improved horizontal resolution, we compare the expected trace gas absorptions of
      small/medium volcanic plumes for different satellite instruments. As a reference, we take the GOME-2 instrument, because

55   from GOME-2 observations it was possible for the first time to observe enhanced BrO amounts for several volcanic plumes
      (Hörmann et al., 2013). A typical detection limit for the SO_2 SCD in the SO_2 standard fit range (about 312 to 324 nm,
      Hörmann et al., 2013; Theys et al., 2017, 2021b) is about 1×10^{16} molec/cm². The detection limit is similar for the different
      instruments, but depends slightly on the signal to noise ratio (see Theys et al., 2019). A SCD of 1×10^{16} molec/cm²
      corresponds to a differential SO_2 optical depth of about 0.001 when measured with a FWHM of about 0.5 nm, like for the

60   TROPOMI instrument. We will use this optical depth as detection limit for SO_2 in this study. This choice is of course a little
      bit arbitrary, but it will serve as a realistic reference point. The detection limit will probably improve in the future using
      advanced analyses techniques, see e.g. the recent study by Theys et al. (2021a).

      If we use the above mentioned SO_2 SCD of 1×10^{16} molec/cm² for a GOME-2 observation (as a reference case) and assume
      that the horizontal extension of observed volcanic plume is smaller than a TROPOMI ground pixel, we can estimate the SO_2

65   SCDs observed for instruments with different ground pixel sizes assuming that the measured SCD scales according to the
      geometric coverage of the volcanic plume. We will see later (light mixing effect) that assuming simple geometry does not
      perfectly describe these observations, but nevertheless provides a good estimate for the overall effect. The resulting SO_2
      SCDs for the different satellite ground pixels are shown in Table 1. The SO_2 SCD for TROPOMI can be higher than the SO_2
      SCD for GOME-2 observations by more than 2 orders of magnitude. Even compared to OMI the increase is larger than a

70   factor of 10.

      The results of these simple calculations indicate the great potential of TROPOMI observations for the detection of
      small/medium volcanic plumes: many weak plumes on the scale of TROPOMI ground pixels were invisible for previous
      sensors. The corresponding increase in the frequency of detection is difficult to quantify, because the exact frequency
      distribution of plume sizes and amounts of SO_2 and aerosols is not known. In addition, also the self-shielding of plumes by

75   aerosols or clouds formed from the plume probably depends on the plume sizes themselves. Nevertheless, we can quantify
      the increase in the detection frequency from the satellite observations themselves. For example, Hörmann et al. (2013) found
      220 volcanic SO_2 plumes per year in GOME-2 data, whereas Warnach (2022) found 870 SO_2 plumes per year in TROPOMI
      data (both studies cover different time periods). In view of the SCD ratios discussed above (see Table 1), this increase by a
      factor of about 4 in the detection frequency seems rather small (see also Theys et al., 2019). The main and simple reason for

80   the small increase of the number of detections is that many volcanic plumes are larger than the size of a TROPOMI pixel.
      For such plumes, the SO_2 SCD detected by TROPOMI will be similar to those for the observations with larger ground pixels.
      However, another reason for the rather low increase of detections is related to 3D effects which are the topic of this paper.
      As shown below, for TROPOMI observations, 3D effects can cause an underestimation of the true plume amount by more
      than 50 % (light mixing effect). For plumes with strong SO_2 absorptions, the underestimation can become even larger.

85   3D effects are fundamental effects and do not only affect UV/vis satellite observations with small ground pixel sizes like
      TROPOMI. However, for instruments with large ground pixel sizes, 3D effects are typically much smaller than for
      TROPOMI, and the related errors are typically ignored, because they are smaller than other measurement uncertainties (e.g.

related to aerosols or the layer height). For small ground pixel sizes (like for TROPOMI), however, the importance of 3D effects increases because of the following reasons:

90 1) the horizontal pixel dimensions are typically smaller (except for situations with low visibility) than atmospheric photon path lengths (see table 1). Thus light scattered horizontally across the borders of the satellite ground pixels becomes important.

2) the horizontal pixel dimensions are smaller than the vertical extent of the troposphere. Thus geometric effects related to slant illumination and viewing geometry become important.

95 3) the horizontal pixel dimensions are similar to those of volcanic plumes. Thus the relative contribution of photons from the sides of the plume increases.

4) one TROPOMI ground pixel might cover the very early part of a volcanic plume, for which the SO_2 concentration can be extremely high. Due to the strong absorption photons will then not penetrate the full plume.

Based on these general aspects, different specific 3D effects can be deduced. In this study we investigate and quantify four

100 specific 3D effects. Two of them (light mixing effect and geometrical effect) were already investigated by Schwärzel et al. (2020, 2021) for ground based and aircraft measurements of NO_2. In this study, we extend these investigations to satellite observations (with different ground pixel sizes). We also investigate two additional 3D effects (saturation effects and plume side effects). The four specific 3D effects are described in more detail below (see also Fig. 2):

a) Light mixing effect: part of the detected photons originates from air masses outside the observed ground pixel (and also

105 from outside the trace gas plume). This leads to a reduction of the trace gas absorption compared to the scenario of a horizontally extended plume (Fig. 2a). Here it should be noted that in case of spatially varying surface albedo or aerosol distributions, the light mixing effect will be increased, which is especially important for aerosol retrievals from satellite (Richters, 1990; Lyapustin and Kaufman, 2001). Also the contributions from different parts within the ground pixel depend on the brightness distribution within the pixel. But here we focus on scenarios with constant surface albedo.

110 b) Saturation effect (Fig. 2b): for strong trace gas absorptions (especially for SO_2 in volcanic plumes) the exact spatial extent of the plume (depending e.g. on the mixing with air from outside) becomes important. If e.g. a trace gas amount is confined in a small part of the satellite ground pixel, the absorption in that part can become very strong. In extreme cases the backscattered light intensity can even approach zero. Then all light measured by the satellite will originate from the remaining part of the satellite ground pixel (outside the narrow plume) where no SO_2 absorption takes place. In such extreme

115 cases, no trace gas absorption will effectively be observed by the satellite. If instead the same amount of molecules is distributed over a larger volume (and thus a larger fraction of the satellite ground pixel), an increased (but typically still too small) SO_2 aborption will be seen. Thus the effective trace gas absorption systematically depends on the horizontal extend of a plume and thus on the temporal evolution of the plume and its mixing with air from outside.

c) Geometric effects: for TROPOMI, the ground pixel size is smaller than the vertical extent of the troposphere. Thus,

120 especially for elevated plumes, geometric effects caused by slant viewing directions and/or slant solar illumination angles can cause a smearing-out and apparent displacement of the volcanic plume compared to its true location. In extreme cases, even double plumes might result (Fig. 2c).

d) Plume side effects: especially if aerosols are present within the plume, edge effects can become important. Their importance increases with decreasing plume size, because a larger fraction of the measured light then reaches the detector

125 from the sides of the plume compared to the top (Fig. 2d). The plume side effect includes the light mixing effect, but adds the dependence on illumination and viewing angle.

Usually all four effects occur for satellite observations at the same time. But in this study we investigate them seperately in order to assess their importance for specific measurement scenarios. For these investigations we use the 3D Monte Carlo model TRACY-2 (Wagner et al., 2007; Kern et al., 2010).

130   It should be noted that for ground based measurements, a fifth 3D effect becomes importat, the so-called light dilution effect
       (Kern et al., 2010). It has contributions from the light mixing effect, but is mainly caused by light scattered into the line of
       sight of the instrument between the plume and the instrument without having crossed the (localised) trace gas plume. Since
       for satellite observations, the observed light typically has not traversed the whole atmosphere, but part of it is scattered above
       the trace gas layer (leading to air mass factors (AMFs) below unity; for the difinition of the AMF, see section 2), the light
135   dilution effect is already implicitely considered in radiative transfer simulations (even in calculations of 1D AMFs). In this
       study the light dilution effect is thus explored as a separate effect only for ground based observations.

       The paper is organised as follows. In section 2 the 3D Monte-Carlo radiative transfer model TRACY-2 is introduced.
       Sections 3 to 6 present simulations of the above mentined four 3D-effects. Section 7 discusses 3D-effects for ground based
       observations, and section 8 presents a summary and outlook.

140

2 The Monte Carlo radiative transfer model TRACY-2

       The Monte Carlo radiative transfer model TRACY-2 was developed by Tim Deutschmann at University of Heidelberg,
       Germany. TRACY-2 allows the simulation of individual photon paths between the Sun and an observing instrument with
145   flexible boundary conditions. The location and properties of the detector (e.g. width and shape of the field of view, FOV) can
       be freely chosen. The atmospheric properties, especially the trace gas and aerosol distributions, can be varied in all three
       dimensions. TRACY-2 is based on the backward Monte Carlo method: a photon emerges from a detector and undergoes
       various interactions in the atmosphere until the photon leaves the top of the atmosphere (where it is 'forced' into the sun with
       appropriate weighting factors). A large number of random photon paths is generated reproducing the light contributing to the
150   simulated measurement. Depending on the atmospheric conditions and the FOV, the number of simulated photons in this
       study ranges from 10 thousand to 1 million. Air mass factors (AMFs) are derived from the modelled radiances with (I) and
       without (I_0) the absorber of interest:

$$AMF = \frac{\ln\left(I_0 / I\right)}{VCD \cdot \sigma} \tag{1}$$

155
       with σ being the absorption cross section of the considered trace gas and VCD the vertical column density (the vertically
       integrated trace gas concentration). Good agreement between TRACY-2 and other radiative transfer models was found in an
       extensive comparison exercise (Wagner et al., 2007). In Fig. 3 an exemplary simulation with TRACY-2 is shown for a
       TROPOMI observation of an idealised narrow plume.

160   For the simulations, an atmospheric domain extending ±20° in latitude and longitude around the plume location (centered at
       0° longitude and 0° latitude) and from the surface to 1000 km altitude is chosen. The horizontal resolution is high close to
       the center (500 m from the center until 10 km) and coarser outside (11.1 km until 111 km; 55.5 km until 555 km, and one
       grid cell from 555 km to 20°). For some simulations (see Figs. 4 and 20) even a finer horizontal grid was used to investigate
       the effect of very narrow plumes (100 m until 22.5 km, 55.5 km until 555 km). The vertical resolution was set to 200 m
165   below 6 km, 1 km until 25 km, 2 km until 45 km, and 5 km until 100 km altitude, and one layer from 100 km to 1000 km.
       The surface albedo was set to 5%. Vertical profiles of temperature, pressure and O_3 concentration are taken from the US
       standard atmosphere (United States Committee on Extension to the Standard Atmosphere, 1976).

       The satellite instrument is placed at 824 km above sea level representing the altitude of the TROPOMI instrument. For the
       investigation of the effects of very narrow plumes (Figs. 4 and 20) as well as for the plume scans (like in Fig. 5) a narrow
170   FOV of 0.014° (corresponding to a ground pixel diameter of 200 m) is used. For the simulations of real satellite

measurements, rectangular FOVs corresponding to the nominal ground pixel sizes of the different satellite instruments are used.

Volcanic plumes are defined for SO_2, BrO, and IO based on ground based and satellite observations (for details see section 2.1). Simulations are performed for selected wavelengths relevant for the considered trace gases: for SO_2, four wavelengths
175 (313.1, 324.15, 332.0, 370.3 nm) are chosen for the dominant absorption bands of the different fit ranges (Theys et al., 2017). Simulations for BrO are performed at 340 nm, and for IO (and NO_2, and H_2O) at 440 nm. Note that substantial amounts of NO_2 are not expected in volcanic plumes. Also, the increase of the atmospheric waper vapor absorption due to water vapor inside the volcanic plume is expected to be very small. Nevertheless, because NO_2 and H_2O are often analysed in the same spectral range as IO, the IO results are also representative for H_2O and NO_2 observations if the ratios of the
180 respective differential cross sections in the spectral range around 440 nm are applied (see section 2.1.3 and appendix A1). Thus the IO results could also be used for the potential detection of enhanced NO_2 or H_2O in volcanic (or other emission) plumes.

AMFs are calculated according to equation 1 for single wavelengths ('monochromatic AMFs'). Thus the wavelength dependence of the AMF (Marquardt et al. 2000; Puķīte et al., 2010, 2016) is not explicitly taken into account, which for
185 strong absorbers usually causes an overestimation of the monochromatic AMFs compared to the true AMFs. In a case study (section 4.3) the effect of the wavelength dependence of the AMF was investigated. It was found that the wavelength dependence of the AMF is negligible for most scenarios (with weak absorptions) considered here. Only for scenarios with strong SO_2 absorptions (with optical depth larger than 0.05 to 0.1) the wavelength dependence of the AMF becomes important and further amplifies the underestimation of the true AMF. But such scenarios can easily be identified and
190 excluded from the data analysis, and for such scenarios wavelengths with weaker SO_2 absorptions should be selected. Thus, the effect of the wavelength dependence of the AMF is ignored in this study, and the main findings can be derived from monochromatic AMFs (equation 1). While this strongly reduces the computationally effort, the computation time for the 3D simulations still remains rather high. The calculation of a single monochromatic 3D AMF takes about 5 min on a state of the art notebook.

195

2.1 Selected trace gas scenarios

The construction of realistic trace gas scenarios is a challenging task. The assumed trace gas plumes should represent realistic distributions, which are based on ground based observations. They should also fit to satellite observations of narrow
200 plumes, which, however, are often close to the detection limit, because the plumes only cover part of the satellite ground pixel. From the satellite observations no information on the sub-ground pixel scale can be obtained.

For this study, trace gas scenarios were set up for SO_2, BrO, and IO. BrO and IO are typically weak absorbers with absorption optical depths clearly below 0.1. Thus they do not significantly affect the atmospheric light path distribution, and only the relative spatial distribution, but not the absolute trace gas amount is important for the calculation of the AMFs.
205 The trace gas scenarios defined below will be used to decide whether the trace gas absorption of a given measurement scenario will be above the detection limit or not. For that purpose we also chose the following detection limits: optical depths of 0.0005 for BrO and IO, and 0.001 for SO_2. Of course these choices are somehow arbitrary, but represent realistic reference points for single observations. Here it should be noted that in some cases (e.g. for continous degassing volcanoes and stable wind fields) many observation might be averaged. In such cases the detection limits will decrease for the
210 statistical mean. Also, for possibly improved future algorithms and instruments more observations are expected to become significant. Thus the results obtained in this study should be seen as a general orientation. The differential cross sections (high-frequency amplitudes) used to convert the SCDs of the different trace gases into optical depths are given in Table A1.1 in the appendix A1.

2.1.1 Size of the volcanic plumes

215

Plume diameters close to volcanic vents are typically ≤1 km (see e.g. Bobrowski et al., 2003; Bobrowski and Platt, 2007; Dinger et al., 2021). Thus we assume as a standard scenario a plume with an extension of 1 x 1 x 1 km³. Of course this is a simplification, since realistic plumes close to the volcanic vent will be more complex (including e.g. a vertical updraft above the vent, and a horizontal outflow part). But here we are interested in the basic effects. In addition to the standard scenario, we also assume plumes with larger horizontal extensions, but with the same vertical extent and the same total amount of molecules. This allows us to study the light mixing effect and saturation effect depending on the turbulent dilution state of the plume. For simplicity we assume that the dilution will only occur in the horizontal dimensions. We investigate plumes in three altitude ranges: 0-1 km, 5-6 km, and 10-11 km.

220

225

2.1.2 BrO

Maximum BrO SCDs measured from ground range up to $1.4 \cdot 10^{15}$ molec/cm² (Bobrowski et al., 2003; Bobrowski and Platt, 2007; Bobrowski and Giuffrida, 2012). However, because of the sparseness of these observations, the maximum occurring BrO SCDs will probably be higher, and we use in the following a maximum value of $5 \cdot 10^{15}$ molec/cm² (for the ‚standard plume' of 1 x 1 x 1 km³). Applying simple geometric consideration, this results in a VCD of $2.6 \cdot 10^{14}$ molec/cm² for a TROPOMI observation with a ground pixel size of 3.5 x 5.5 km² (assuming that for the ground based measurements the SCD equals the VCD, i.e. assuming that the ground based telescope is directed towards the zenith). This value is similar to maximum BrO VCDs observed by TROPOMI for narrow plumes (plumes with extensions of a TROPOMI ground pixel or less). For such cases, Warnach (2022) observed BrO VCDs up to about $2.5 \cdot 10^{14}$ molec/cm² (assuming a 1D-AMF of 0.5 corresponding to plumes close to the surface). The BrO scenario corresponds to a total number of BrO molecules in the standard plume (1 x 1 x 1 km³) of $5 \cdot 10^{25}$. An overview about the corresponding BrO VCDs for the different horizontal plume extensions is given in Table 3.

230

235

2.1.3 IO

240

Also IO is a weak absorber, but because of the sparseness of IO observations in volcanic plumes (e.g. Schönhardt et al., 2017), we simply use the same VCD ($5 \cdot 10^{15}$ molec/cm²) as for BrO for the standard plume (1 x 1 x 1 km³) corresponding to a VCD of $2.6 \cdot 10^{14}$ molec/cm² for a TROPOMI observation. This value probably overestimate the true IO amounts in volcanic plumes. But since IO is a weak absorber, the results are representative also for plumes with smaller IO amounts.

245

The corresponding VCDs for the different horizontal plume extensions are shown in Table 3.

The results of the IO scenarios could be also transferred to measurements of NO_2 and H_2O, if they were analysed in the same spectral range (around 440 nm). To convert the IO results to the corresponding NO_2 and H_2O results, just the ratios of the cross sections have to be applied. With a (differential) absorption cross section of $3 \cdot 10^{19}$ cm² for NO_2, and $3 \cdot 10^{26}$ cm² for H_2O (see table A1.1), all IO VCDs and SCDs would have to be multiplied by 83 and $8.3 \cdot 10^{8}$ for NO_2 and H_2O, respectively. The IO VCD for the standard plume ($5 \cdot 10^{15}$ molec/cm²) corresponds to a NO_2 VCD of $4.15 \cdot 10^{17}$ molec/cm² and a H_2O VCD of $4.15 \cdot 10^{24}$ molec/cm².

250

2.1.4 SO_2

255

SO_2 absorptions of volcanic plumes can cover a wide range. SO_2 can act as weak, but also as a very strong absorber, depending on the one hand on the amount of molecules in a plume, which can vary over many orders of magnitude. On the other hand it strongly depends on the selected wavelength range. At short wavelengths, the SO_2 absorption cross section is much stronger than at longer wavelengths. Around 310 nm, the absorption cross section is about $3.5 \cdot 10^{-19}$ cm², around 320

260   nm about $5 \cdot 10^{-20}$ cm², around 330 nm about $2 \cdot 10^{-21}$ cm², and around 370 nm $6 \cdot 10^{-22}$ cm² (see Fig. 6).

The standard wavelength range for the TROPOMI SO_2 analysis is 312 to 326 nm (Theys et al., 2021b). This wavelength range is especially well suited for plumes with small SO_2 amounts. For the scenario with SO_2 as a weak absorber we chose a VCD of $1 \cdot 10^{18}$ molec/cm² for the standard plume (1 x 1 x 1 km³). For a TROPOMI observation this corresponds to a VCD of $5.2 \cdot 10^{16}$ molec/cm² and an optical depth of about 0.002 (around 313 nm, see table A1.1).

265   In addition to this scenario, we also consider 4 scenarios with SO_2 as a strong absorber (in the standard TROPOMI fit range). The maximum SO_2 VCD is chosen according to Kern et al. (2020), who observed a very high SO_2 VCD (about 2 to $3 \cdot 10^{20}$ molec/cm² over an about 2 km wide plume from the Kilauea volcano about 4 km downwind of the vent. Thus we use a VCD of $4 \cdot 10^{20}$ molec/cm² as maximum VCD for the standard plume (1 x 1 x 1 km³). A very high SO_2 SCD of $3.2 \cdot 10^{19}$ molec/cm² was also observed by Bobrowski et al. (2010). Very high SO_2 VCDs up to $5 \cdot 10^{19}$ molec/cm² were also observed

270   by TROPOMI for the La Palma eruption in Summer 2021 (e.g. Warnach, 2022). Here the plume usually covered several TROPOMI ground pixels, but with maximum SO_2 VCDs for individual TROPOMI pixels indicating a characteristic horizontal plume extension similar to a TROPOMI pixel. To cover a large range of strong SO_2 absorptions, we chose the following VCDs (for a 1 x 1 x 1 km³ plume): $1 \cdot 10^{19}$ molec/cm², $2.5 \cdot 10^{19}$ molec/cm², $1 \cdot 10^{20}$ molec/cm², and $4 \cdot 10^{20}$ molec/cm². The corresponding VCDs for the different SO_2 scenarios and horizontal plume extensions are given in Table 3.

275   The standard fit range is represented by simulations at 313.1 nm (where the strongest SO_2 absorption peak is located). In addition, also simulations at 324.15 nm, 332.0 nm, 370.3 nm are performed. The corresponding optical depths for the chosen wavelengths are summarised in Table 4.

2.2 Aerosol input data

280

For the investigation of aerosol effects two scenarios are considered. For both scenarios an aerosol optical depth (AOD) of 10 (for the 1 x 1 x 1 km³ plume) is assumed, either with purely scattering aerosols (SSA = 1) or strongly absorbing aerosols (SSA=0.8). The first case represents plumes with sulfuric acid aerosols, the second case plumes with ash particles. The phase function is represented by the Henyey-Greenstein model with an asymmetry parameter of 0.68. These simplified scenarios

285   were chosen to represent the basic characteristics of aerosol containing volcanic plumes. It should be noted that there is a lack of observations of the total amount of aerosols in fresh plumes, mainly because the high AOD in such situations itself prevents accurate measurements of the AOD. Like for the trace gases, also the aerosol amount is kept constant for the different horizontal plume extension leading to different AODs for different horizontal plume extensions (see table 3).

3 Light mixing effect

290

The effect of horizontal light paths on satellite observations has first been investigated for aerosol retrievals from satellites (Richter, 1990; Lyapustin and Kaufman, 2001). Such retrievals are based on radiance measurements, and the effect of horizontal light paths can strongly affect the measurements in the presence of strong spatial radiance contrasts, e.g. caused

295   by sea-land boundaries or cloud edges. In such cases, horizontal light paths cause an increase (decrease) of the radiance above the dark (bright) scene and thus systematically affects the aerosol retrieval. This effect (for absolute radiance measurements) was referred to as adjacency effect (Richter, 1990).

Trace gas measurements are usually not based on absolute radiance measurements but on narrow-band relative (differential) absorptions. Also for such measurements, horizontal light paths can play an important role. But in contrast to aerosol measurements (based on absolute radiances), horizontal light paths affect the measurements even for scenes without spatial radiance contrasts (if spatial gradients of the trace gas of interest are present). In order to distinguish the effect of horizontal light paths on trace gas measurements from those on absolute radiance measurements (adjacency effect), we refer to it in this study as light mixing effect.

Light mixing effects for trace gas measurements have first been investigated by Schwärzel et al. (2020; 2021) for ground based and aircraft measurements. They found that like for the aerosol measurements, the light mixing effect for trace gas measurements causes a spatial smoothing of the trace gas signals.

Here we extend these investigations to satellite observations. First we investigate the fundamental effects of horizontal photon paths (for scenarios without aerosols). Then we quantify the light mixing effect for ground pixel sizes of different satellite sensors and also scenarios with aerosols taking into account also realistic detection limits.

3.1 General findings and dependencies of the light mixing effect for trace gas observations

Fig. 4 presents trace gas AMFs for different plume altitudes and wavelengths as function of the horizontal plume extension. The vertical plume thickness is 1 km. The wavelengths were chosen to represent typical trace gas analyses relevant for volcanic studies (SO_2 around 313 nm, BrO around 340 nm, IO around 440 nm, see section 2.1). The AMFs strongly depend on the horizontal plume extension. This dependency gets stronger towards shorter wavelengths, because of the higher probability of Rayleigh scattering and thus a larger contribution of photons originating from outside the satellite's FOV. Interestingly, the normalised AMFs (divided by the corresponding 1D AMFs) for different altitudes show a similar dependence on the horizontal plume extension indicating compensating effects of the increasing free path lengths and the decreasing scattering probability with increasing altitude (because of the decreasing air density). The results in Fig. 4 show that the light mixing effect can cause a strong underestimation of the trace gas amounts of a volcanic plume if a 1D AMF is used in the data analysis. The underestimation is largest for small plumes and short wavelengths (up to > 70%).

In Fig. 5 so-called plume scans for plumes with different horizontal extensions are presented. The highest AMFs occur directly above the plume center, but even these AMFs are systematically smaller compared to the corresponding 1D AMFs (orange horizontal lines). The deviation is strongest for short wavelengths and narrow plumes. The AMFs slightly decrease from the plume center towards the edges. Outside the plume they decrease rapidly, but stay clearly above zero.

This 'smoothing' of the AMF (compared to the horizontal extent of the plume) reflects the effect of horizontal photons paths and is directly connected to the atmospheric visibility. Towards short wavelengths, the free photon paths get shorter and the scattering probability gets higher. Thus the smoothing effect is strongest at short wavelengths.

One interesting question is whether the decrease of the AMF above the plume (compared to the 1D AMF) and the increase outside the plume (compared to a zero AMF) exactly compensates each other. Indications for such a compensation are illustrated in Fig. 7 (note that for a quantitative interpretation, two horizontal dimensions have to be considered). To answer this question, simulations for satellite observations with a very large FOV corresponding to a ground pixel size of 200 x 200 km² are performed. Such large ground pixels are larger than typical horizontal photon paths (see Table 2). Thus almost all photons which have 'seen' the trace gas plume will stay inside the FOV.

The simulation results (together with similar results for a TROPOMI FOV) are shown in Fig. 8. The top panels present the detected fraction of the plume amount (using a 1D AMF) as function of the horizontal plume extension. The detected fraction of the plume amount is calculated as follows: First the simulated SCD for 3D plumes is divided by the corresponding 1D AMF yielding the average VCD across the satellite ground pixel. This VCD is then multiplied by the area

340   of the ground pixel size yielding the total number of molecules. Finally, this value is divided by the number of trace gas
molecules used as input for the simulations.

For TROPOMI, the retrieved fractions of the plume amount largely underestimate (by >50%) the input trace gas amounts for
small plume sizes, in agreement with the results shown in Figs. 4 and 5. The largest underestimation occurs for a plume size
similar to the ground pixel size. This can be understood by the results of the plume scans shown in Fig. 5, where the AMFs

345   at the plume edges are the smallest within the plume. For plumes larger than the TROPOMI ground pixel, the retrieved
fraction of the plume content (within the ground pixel size) then increases with plume size, because these scenarios converge
to the 1D scenario (horizontally homogeneous trace gas layer).

Interestingly, for the large FOV (corresponding to a satellite ground pixel of 200 x 200 km²) the retrieved fractions of the
plume amount is close to unity independent from the plume size. This confirms the above expectation that the decrease of

350   the AMF in the area of the plume (compared to the 1D AMF) and the increase of the AMF outside the plume (compared to
zero) compensate each other. In conclusion we find that the correct plume amount can be retrieved using 1D AMFs only for
two extreme cases:

a) The ground pixel size is much larger than the free photon path length and the plume size (Fig. 8 right). However, in such
cases the trace gas absorption is very weak and usually below the detection limit (see Fig. 8 bottom right). Thus

355   small/medium volcanic plumes can usually not be detected by instruments with a large ground pixel size.

b) The plume size is much larger than the free photon path length (and the ground pixel size). This is typically fulfilled for
strong eruptions. But such plumes are large and can usually be detected by satellite instruments with low spatial resolution
(no observations with high spatial resolution are needed).

Thus small plumes (like for small/medium volcanic eruptions or degassing events) can only be observed by sensors with a

360   small ground pixel size (like TROPOMI). But for such observations the retrieved trace gas amount will be systematically
and strongly underestimated if 1D AMFs are applied in the data analysis.

3.2 Quantitative analysis for different ground pixel sizes taking into account the detection limit of the spectral retrieval

365

As shown in the previous section, all molecules of a volcanic plume could in principle be retrieved with a 1D AMF if the
satellite ground pixel would be large (> about 100 x 100 km²). Thus, even for satellite measurements with small ground
pixels it should be possible to retrieve all molecules of a volcanic plume if the results of many neighboring ground pixels
(surrounding the volcanic plume) were summed up. However, since the AMFs for pixels outside the volcanic plume are

370   typically rather small (Fig. 5), for most of the observations of neighboring ground pixels the trace gas absorption will be
below the detection limit. This finding is confirmed in Fig. 9, which shows simulation results for the trace gas scenarios for
the weak absorbers introduced in section 2.1. Here again it should be noted that these results are valid only for the assumed
trace gas scenarios and detection limits. For higher plume amounts and/or lower detection limits, lower SCDs, e.g. those for
the neighboring pixels might be above the detection limit. Moreover, for scenarios with constant emissions (degassing) and

375   stable wind fields, several measurements could be averaged, which would also lower the detection limit which is usually
determined by photon noise. Nevertheless, from these simulations we derive the following general conclusions:

a) The trace gas SCDs from neighboring pixels are usually rather small. For TROPOMI observations the ratios of the
maximum SCDs from the neighboring pixels relative to the SCDs of the center pixel range from 2% for 440 nm to 8% for
313 nm. Thus these measurements will often be below the detection limit.

380   b) even if measurements of the neighboring pixels are above the detection limit, their contribution to the detected total plume
amout is small. For the two closest neighboring pixels (because of symmetry in total 4) their additional contribution ranges
from about 6% (440 nm) to about 16% (313 nm).

c) for OMI, SCIAMACHY, or GOME-2, the SCDs of the neighboring pixels are always below the detection limit for the scenarios (with narrow volcanic plumes) considered here (see Table 3).

385 Fig. 10 shows the retrieved fraction of the plume molecules (for a 1 x 1 x 1 km³ plume between 5 and 6 km altitude) as function of the ground pixel size for the three selected wavelengths. As discussed before, the strongest underestimation is found for TROPOMI and for short wavelengths. For SCIAMACHY and GOME-2 observations, the underestimation is only between a few and 15 percent. However, for these sensors the retrieved trace gas SCDs are below the detection limit for the narrow plumes considered here. Interestingly, very similar results are found for 313 and 340 nm, probably because of some

390 compensating effects of the increase of the light mixing effect, but also an increase of the probability for multiple scattering towards shorter wavelengths. For plumes close to the surface (0 - 1 km altitude) very similar fractions are found (not shown) as for the plume between 5 and 6 km, but because of the decreasing sensitivity of the satellite observations towards the ground, the corresponding trace gas absorptions are smaller and for the weak SO_2 scenario even below the detection limit.

395 **3.3 Influence of aerosols**

Fig. 11 presents AMFs (similar to Fig. 5) and normalised radiances (radiance/irradiance) for plume scans in near-nadir viewing geometry (solar zenith angle, SZA=0°) for different wavelengths and aerosol scenarios. The plumes are located between 5 and 6 km and contain the trace gas together with the aerosols. Again the plume content is assumed to be constant,

400 that the trace gas VCDs and AOD vary with the horizontal plume extent (see Table 3). The aerosols are assumed either purely scattering (SSA=1) or strongly absorbing (SSA=0.8). The different colours in Fig. 11 represent AMFs and normalised radiances for plumes with different horizontal extensions (from 1 x 1 km² to 40 x 40 km²).

For small plume extensions (and thus high aerosol extinction in the plume) a strong effect of aerosols is seen: for the scenarios with scattering aerosols, both the AMF and the normalised radiance increase compared to the scenarios without

405 aerosols (Fig. 5). For the scenarios with absorbing aerosols the opposite is found. For the interpretation of the simulated radiances it is important to take into account that a substantial fraction of the atmospheric molecules is still located above the volcanic plume, which scatter the sun light towards the instruments without having 'seen' the plume. Thus even for narrow plumes with absorbing aerosols the reduction of the observed radiance above the plume is relatively small. The low radiances at 313 nm are caused by the stratospheric ozone absorption, which is negligible at longer wavelngths.

410 For observations with extended FOV, the effective AMF results from the spatial averaging of the AMF weighted by the radiance. In that way the increased (decreased) radiance above scattering (absorbing) aerosols further increases (decreases) the AMFs for scattering (absorbing) aerosols. As a consequence, aerosols can have a rather strong impact on the effective AMF compared to the scenarios without aerosols.

In Fig. 12 the retrieved ratios of the plume amount for TROPOMI observations are shown for aerosol scenarios (for a 1 x 1 x

415 1 km³ plume). Compared to the results for the aerosol-free cases the results are higher (for scattering aerosols) or lower (for absorbing aerosols). For scattering aerosols, the plume amount can even be overestimated caused by the light path enhancement due to increased multiple scattering in the plume as well as more backscattered light from the plume (higher reflectance above the plume). Very similar to the scenarios without aerosols, the ratios of the maximum SCDs of the neighboring pixels to the SCDs of the center pixels range from 2 % to 9.

420

4 Saturation effect

For strong atmospheric absorbers like SO_2, the exact plume extent becomes especially important. If the same amount of molecules is confined in a small or large volume (depending on the dilution state of the plume), the corresponding VCDs and

425 vertical optical depths vary. For narrow horizontal plume extensions (e.g. in fresh plumes before effective mixing with

ambient air) the optical depth is higher than for more diluted plumes (Fig. 2b). This effect is illustrated in Fig. 13 for SO_2 observations at a wavelength of 313 nm (representative for the standard SO_2 fit range, see Fig. 6). In the left part of the figure the spatial distributions of the SO_2 VCDs are shown for the scenarios with SO_2 as weak absorber (top), ‚strong,1' (middle), and ‚strong,4' (bottom), see table 3. The different colours indicate the different horizontal extensions of the plume

430 (with the total amount of molecules kept constant). In the center and right part of the figure, plume scans of the AMF and the backscattered normalised radiance are shown. As expected, for the scenario with SO_2 as weak absorber even for the smallest horizontal plume extension (1 x 1 km²) the radiance above the plume is the same as outside the plume (top, right). The decrease of the AMF compared to the 1D-AMF is thus simply a result of the light mixing effect (section 3). For higher SO_2 concentrations, however (middle and bottom panel), the radiance is systematically reduced above the plume (like for the

435 scenario with strong aerosol absorption, see Fig. 11 bottom), because a substantial fraction of the photons is absorbed by SO_2. Here it is interesting to note that even for the highest SO_2 concentrations the radiance does not approach zero indicating that part of the light is backscattered from molecules above the volcanic plume (while almost all photons reaching the volcanic plume are probably absorbed by SO_2). Accordingly, with increasing plume height a stronger reduction of the observed radiance for plumes with high SO_2 amounts is found. For the scenarios with high SO_2 amounts, also the AMFs

440 above the plume are systematically reduced compared to the scenarios with weak SO_2 absorption, because the SO_2 absorption is so strong that the observed photons have only ‚seen' part of the vertical plume extension (similar to the scenario with strong aerosol absorption, see Fig. 11 bottom). The combined effects of reduced backscattered radiance and reduced AMFs strongly reduces the effective AMFs, when averaged over a satellite ground pixel. The reduction of the AMF is largest for the narrow plumes.

445

4.1 SO_2 results for TROPOMI observations for different plume contents and wavelengths

Fig. 14 shows the fraction of the retrieved plume molecules as function of the plume size derived from TROPOMI observations if a 1D-AMF is assumed in the analysis. In addition, the retrieved SO_2 SCDs are shown. The simulations are

450 performed for the 4 scenarios with strong SO_2 absorption (see table 3) and 4 wavelengths (313.1 nm, 324.15 nm, 332.0 nm, 370.3 nm, see table 4 and Fig. 6). From the results in Fig. 14 several conclusions can be drawn:

a) a systematic and strong underestimation for short wavelengths is found (in addition to the light mixing effect). This additional underestimation is caused by the strong SO_2 absorption for narrow plumes and is referred to in this study as saturation effect.

455 b) in spite of the strong SO_2 absorption, in some cases, the retrieved SO_2 SCDs are below the threshold value (red horizontal line), above which the operational SO_2 retrieval switches to the alternative fit windows (at longer wavelengths), see Theys et al. (2021b). This is an important finding, because in such cases no analyses in the alternative fit windows will be performed and such high SO_2 amounts stay undetected in the current TROPOMI SO_2 retrieval.

c) To retrieve the correct SO_2 SCD (and to avoid the saturation effect), it is recommended that simultaneous analyses in

460 different wavelength ranges are performed. If the SCDs at shorter wavelengths are found to be systematically smaller than those at longer wavelengths, the results of the retrievals at the longer wavelengths should be considered. Only if in the standard fit window similar SCDs are obtained as at longer wavelengths, the results from the standard fit window should be used. This procedure would avoid that high SO_2 amounts stay undetected. Specific thresholds for the differences of the results in the different fit windows should be defined in a dedicated and more detailed study taking also into account the

465 increasing detection limits towards longer wavelengths.

4.2 SO_2 results for observations from different satellites

Fig. 15 presents an overview on the retrieved SO_2 amounts by different satellite instruments for scenarios with strong
470 absorptions (see table 3). For all SO_2 scenarios a strong dependence of the retrieved SO_2 SCD (and the fraction of the
retrieved plume molecules) is found. The wavelength above which the underestimation becomes negligible depends on the
SO_2 scenario (see table 3). For high SO_2 amounts, only analyses at long wavelengths yield reasonable results (but are of
course still affected by the light mixing effect). Interestingly, the saturation effect is similar for the different instruments
(with different ground pixels sizes), indicating that the saturation effect is mainly determined by the plume properties.

475

4.3 Effect of the wavelength dependence of the AMF

So far the simulations were performed at single wavelengths in order to save computation time. These wavelengths were
chosen to represent the dominant differential absorption cross sections for the different SO_2 fit windows (see Fig. 6 and table
480 A1.1). While these monochromatic simulations can give a good first indication of the saturation effect, they neglect the
effect of the wavelength dependence of the AMF (Marquard et al., 2000; Puķīte et al., 2010, 2016). This wavelength
dependence is mainly caused by the wavelength dependence of the SO_2 absorption cross section, because for increasing
absorption cross sections the penetration depth of the backscattered photons (and hence the AMF) decreases: the AMF is
smallest for the highest values of the cross sections, and the wavelength-dependence of the AMF leads to a further decrease
485 of the differential optical depth:

$$\tau(\lambda) = VCD \cdot AMF(\lambda, \sigma(\lambda)) \cdot \sigma(\lambda) \qquad (2)$$

Note that an additional wavelength dependency of the AMF due to Rayleigh scattering is less important for the rather small
490 fit windows considered here. We quantify the effect of the wavelength dependence of the AMF as described in appendix A2.
It is found that the effect of the wavelength dependence of the AMF is small for cases with small optical depths. For cases
with high optical depths and thus strong saturation effects, the true underestimation becomes larger than for the
monochromatic AMFs. But such cases can be easily identified by the comparison of the retrieved SO_2 SCDs from different
spectral ranges. For the SO_2 analysis, then an appropriate spectral range (with negligible saturation effect) has to be selected.
495 For such analyses, also the effect of the wavelength dependence of the AMF becomes negligible.

5 Geometric effects

The simulations presented so far were carried out for scenarios with overhead sun (SZA = 0) and nadir-looking instruments
500 (viewing zenith angle, VZA = 0). These scenarios were chosen to investigate the light mixing and saturation effects in a
fundamental way. In typical measurement situations, however, the illumination and viewing directions deviate from the
vertical axes. Especially for elevated plumes, the trace gas absorption will then not be seen for the ground pixel exactly
below the plume (Fig. 2c). In extreme cases, even double plumes might be observed. These effects of slant illumination and
viewing angles are referred to as geometric effects in this study and are investigated in this section. Geometric effects lead to
505 an increase of the horizontal extension over which the plume signal is seen compared to the observation geometry with SZA
= VZA = 0. But at the same time, also the magnitude of the absorption is decreased, and might effectively fall below the
detection limit. This reduction of the absorption is simply caused by the fact that for cases with SZA ≠ VZA the atmospheric
light paths cross the plume only once (or less) for a given viewing angle.
In Fig. 16 the AMFs for plume scans for observations of elevated plumes with various combinations of SZA and VZA are
510 shown. The blue lines show the AMFs for observations with a narrow FOV (right y axis); the bright blue horizontal bars
represent simulations for a TROPOMI FOV (3.5 km in across track dimension, left axis). Note that we kept the ground pixel

size constant (3.5 x 5.5. km²) for all viewing angles in order to study the basic effects in a systematic way. For real TROPOMI observations, the ground pixel sizes increase for slant viewing angles. The TROPOMI AMFs are systematically lower than the AMFs for the narrow FOV, because the plume covers only a small fraction of the TROPOMI ground pixel
515 (for nadir view ~5%).

The simulations shown in Fig. 16 are performed for 440 nm. Similar results, but with less clear peaks, are obtained for the other wavelengths (see appendix A3). In addition to the AMFs, also sketches of the corresponding observation geometries are shown above the sub figures. As expected, the plume signals seen by the satellite are usually not found for those ground pixels covering the plume. Instead, maxima of the AMF are found for the downward and upward light paths crossing the
520 plume, but slightly enhanced values are also found in between these maxima. They are caused by sunlight which has crossed the plume and is then scattered towards the instrument before it reached the ground. As a general finding, the apparent horizontal extent of the plume increases for observations with slant illumination and/or slant viewing angles compared to observations with SZA = VZA = 0. At the same time the magnitude of the AMF decreases for observations with slant illumination and/or slant viewing angles. Both aspects have a direct influence on the detected total fraction of the plume
525 amount: on the one hand, the ‚smearing' of the plume signal can lead to a larger number of ground pixels with enhanced absorptions and thus to a larger total covered area. On the other hand, ground pixels with weak absorptions (e.g. between the two AMF maxima) might fall below the detection limit (especially for scenarios with low trace gas VCDs). Both dependencies are seen in Fig. 17 where the number of pixels above the detection limit and the detected total fraction of the plume amount for TROPOMI observations with various viewing and illumination angles are shown for different scenarios of
530 weak absorbers (see table 3). For the different trace gases, different numbers of pixels with SCDs above the detection limit are found. The largest numbers are found for 440 nm (weakest probability of Rayleigh scattering) and slant viewing and illumination angles (with opposite direction, relative azimuth angle, RAA = 0°), for which the apparent spatial extent of the plume gets largest. Interestingly, the detected fraction of the plume amount is similar for all viewing geometries.

535 **6 Plume side effects**

For slant illumination and viewing angles, interactions of photons with the sides of the plumes can become important, especially for plumes containing aerosols. However, even for plumes free of aerosols, photons entering or leaving the plumes from the sides have ‚seen' different trace gas absorptions compared to the 1D scenarios. In this section plume side effects are
540 investigated for TROPOMI observations and for a narrow plume (1 x 1 x 1 km³) located directly above the surface. The aerosol scenarios are similar as in section 2.2 with an AOD of 10 and a single scattering albedo of 1.0 (purely scattering aerosols) or 0.8 (strongly absorbing aerosols). Note that plume side effects play also a role for the scenarios in the previous section on geometric effects. But there the focus was on the horizontal smearing and apparent displacement of elevated plumes.

545 In the middle panels of Fig. 18a,b the AMFs and normalised radiances for plume scans with a narrow FOV (0.014°) for (a) 440 nm and (b) 313 nm are shown (blue symbols). The simulations are performed for a slant viewing angle (VZA = 60°) and selected SZAs (0° and 60° in forward and backward direction). The plumes of 1 x 1 x 1 km³ are located at the surface (red boxes) and contain the trace gas and scattering aerosols with an AOD of 10. In addition to the AMFs for the narrow FOV, also AMFs for a TROPOMI FOV (3.5 km in across track direction) are shown (horizontal magenta bars). Especially for 440
550 nm the normalised radiances and AMFs for the narrow FOV show complex dependencies on the viewing angle. Also clear differences for forward and backward illumination are found. The stronger and more structured signals at 440 nm are caused by the fact that the direct sun light can penetrate more deep into the atmosphere than at shorter wavelengths and thus geometric effects (like shadowing for a VZA of 60° and a SZA of -50°) are more clearly visible. Also the AMFs for the TROPOMI FOV differ systematically for different illumination directions. The TROPOMI AMFs (for ground pixels

555   covering the plume) as function of the SZA and for different aerosol scenarios) are shown in the bottom panels of Fig. 18. Besides the 3D-AMFs also the corresponding 1D-AMF (without aerosols) are presented. A clear dependence on the SZA is found for all AMFs, which is slightly asymmetric (for forward and backward illumination) for the non-nadir viewing direction (VZA = 60°). These dependencies are caused by two effects: first by the angular dependence of Rayleigh scattering which is relevant for both the 1D and 3D simulations; second by the angular dependence of Rayleigh scattering and aerosol

560   scattering (if aerosols are present) for the 3D plumes).

Fig. 19 shows the detected fraction of the plume amount for the different 3D cases if the corresponding 1D-AMF is applied in the data analysis (similar to Fig. 12). For 313 nm and 340 nm only weak dependencies on the SZA are found indicating that at these short wavelengths the direct sun light does not penetrate deep into the atmosphere (because of the high probability of Rayleigh scattering). Also only a weak dependence on the viewing angle is found. The low AMFs for the VZA

565   of 60° are related to the fact that for such slant angles the FOV for a 3.5 km wide ground pixel is rather small, and not the whole vertical extent of the 1 x 1 x 1 km³ plume falls within the FOV.

In contrast to 313 nm and 340 nm, for 440 nm systematic dependencies on the SZA are found, indicating the increased penetration depth of the direct sun light. For plumes without aerosols, almost constant ratios are found for SZA < 70°, while for SZA ≥ 70° the ratios strongly decrease. For observations of 3D plumes under such slant illumination angles part of the

570   direct sun light has not crossed the plume (like for the 1D scenario) before it is reflected / scattered towards the instrument. For the scenario with scattering aerosols, the ratios are always > 1 indicating the effect of multiple scattering (together with the increased radiance from the plume providing more weight for the trace gas signal from the plume). The ratios systematically increase with increasing SZA (except for the highest SZA). This increase is related to the higher contribution of photons entering the plume from the sides (pronounced forward scattering). For the non-nadir observations (VZA ≠ 0)

575   also a slight asymmetric dependence on the SZA is found.

For the scenario with absorbing aerosols, low ratios and almost no SZA-dependence are found indicating that the aerosol absorption prevents the penetration of the solar photons deep into the volcanic plume (together with the reduced radiance from the plume). In summary, as already shown in section 3.3, the 3D-AMFs for plumes with scattering aerosols can be strongly increased compared to aerosol-free plumes. This overestimation is strongest for long wavelengths. In such cases the

580   satellite measurements strongly overestimate the amount of plume molecules if a 1D AMF is applied up to >100% towards high SZA and high VZA. Interstingly, the ratio of the 3D AMF for scattering aerosols versus the 1D AMF (without aerosols) at 313 nm is close to unity regardless of the geometry. For SO_2 measurements of such plumes in the standard fit range, the application of 1D AMFs will thus lead to rather small errors.

For observations of plumes without aerosols or with absorbing aerosols the satellite measurements strongly underestimate

585   the amount of plume molecules if a 1D AMF (without aerosols) is applied in the data analysis (in agreement with the results shown in section 3.3).

7 Ground based measurements

590   Kern et al. (2010) investigated the effect of sun light scattered into the line of sight between the instrument and the volcanic plume. They referred to this effect as light dilution effect. Their simulations were performed with the same radiative transfer model TRACY-2 as used in this study. As a general set up they assumed a plume with a vertical extension of 500 m and a horizontal extension of 600 m located at different altitudes. The instrument was directed to the plume either in slant or vertical direction. The SZA was always 30°. Kern et al. (2010) found that the AMF can be strongly reduced by the light

595   dilution effect. While for plumes directly above the surface, the AMF was similar to the geometric AMF, it strongly decreased with increasing plume altitude.

Atmospheric
Measurement
Techniques
Discussions

In this section we perform similar simulations, but we vary also the horizontal plume extent and the SZA (see Fig. 20). Like for the satellite observations (Fig. 4), a strong and systematic dependence of the AMFs on the horizontal plume extension is found. These results indicate that for ground based observations not only the dilution effect but also the light mixing effect is

600 important. This becomes particularly obvious for the simulation results for SZA = 0° (Fig. 20 top). In these cases (in contrast to the scenarios in Kern et al. (2010)) no direct sun light is scattered into the line of sight between the plume and the instrument, but still a systematic dependence of the AMFs on the horizontal plume extent is found. Like for satellite observations, the strongest dependence of the AMF is found for 313 nm, because the probability of Rayleigh scattering is largest for the short wavelengths. But the altitude dependence is opposite to that for the satellite observations.

605 When comparing the results for SZA = 0° and SZA = 10°, an interesting difference is found for narrow elevated plumes. For 10° SZA, direct sunlight can reach the line of sight of the instrument below the plume without having traversed the plume (dilution effect as in Kern et al., 2010) leading to much smaller AMFs than for the simulations with exact overhead sun (SZA = 0°). Except for these narrow elevated plumes, the results for both SZAs are almost identical indicating that the light mixing effect occurs independently from whether the direct sun light is scattered into the line of sight with or without having

610 crossed the plume before. Or in other words, the light mixing effect is the more fundamental effect, and the dilution effect (if the direct sun light has not crossed the plume before) can further strongly decrease the AMF.

The results of this study indicate that the correction factors presented by Kern et al. (2010) are only valid for the chosen plume size (vertical extent of 500 m, horizontal extent of 600 m). However, an assumed change of the plume extent from 200 m to 4 km changes the AMFs by about 5 % (for 440 nm) and 30 % (for 313 nm). Thus for future analyses of ground

615 based observations, the plume size should be also taken into account.

8 Conclusions

In this study different 3D effects were investigated with a focus on satellite observations. The new TROPOMI instrument

620 aboard Sentinel-5P has a much smaller ground pixel size (down to 3.5 x 5.5 km²) than previous sensors. Thus TROPOMI can detect small volcanic plumes, which were invisible for the precursor instruments. However, for observations with small ground pixels, 3D effects become important, which were of minor importance for the observations with larger ground pixels.

We investigated the following four 3D effects: the light mixing effect caused by horizontal photon paths, the saturation effect caused by strong SO_2 absorption, geometric effects related to slant illumination and viewing angles, and side-

625 scattering effects related to photons originating from the sides of volcanic plumes.

Especially the first two effects can lead to a strong and systematic underestimation if 1D assumptions are used in the data analysis (up to more than 50% for the light mixing effect, and up to 100% for the saturation effect). Thus for TROPOMI analyses of small volcanic plumes the light mixing effect has to be considered if the volcanic plume covers only 1 satellite ground pixel (or a small number of ground pixels with a clear maximum for a single ground pixel). In such cases,

630 wavelength-dependent correction factors (according to the results in Fig. 10) have to be applied to the results if a 1D AMF is used.

The saturation effect can lead to a further strong underestimation of the analysis results for cases with strong SO_2 absorptions. In extreme cases, in spite of the strong SO_2 absorption, the SO_2 SCDs retrieved in the standard fit window might even stay below the threshold for the switch of fit windows, and such plumes might remain undetected. For future analyses

635 (not only for TROPOMI, but also for other sensors) we recommend to always retrieve SO_2 SCDs simultaneously in different fit windows. If the SCDs retrieved at short wavelengths (standard analysis) are found to be systematically smaller than at the other wavelengths, the SCDs from the alternative fit windows should be used.

Geometric effects typically have a weaker influence on the quantitative results, but they can affect the spatial pattern under which elevated plumes are ‚seen' by the satellite instrument. Usually, localised elevated plumes are widened and even

640   double peaks can occur. These effects should be kept in mind if complex plume patterns are observed. They might be simply caused by slant viewing and/or illumination angles.

Plume side effects are usually small for short wavelengths, but become larger for longer wavelengths. Especially if scattering aerosols are present in volcanic plumes they can lead to a strong overestimation if 1D AMFs (without aerosols) are used. While this overestimation is rather small for nadir observations and overhead sun (between about 5% and 50% depending on

645   wavelength), it can reach much higher values (up to >100%) for slant viewing and illumination angles. Here it is important to note that such effects will probably play a rather important role for future sensors like the upcoming geostationary Sentinel-4 mission (Bazalgette Courrèges-Lacoste et al., 2017) which measures under rather slant viewing and illumination angles at northern latitudes.

Also for ground based observations, 3D effects can become important. In addition to the dilution effect (see Kern et al. 2010)

650   especially the light mixing effect shows a similar strong dependence on the horizontal plume extension as for satellite observations. Thus the horizontal plume extension should also be taken into account for the analysis of ground based observations.

In this study the most fundamental 3D effects were investigated, but some important questions remain open:

a) How representative are the assumed aerosol properties for real volcanic plumes? There is a huge knowledge gap about

655   aerosol properties in volcanic plumes, mainly because especially for absorbing aerosols, the dense volcanic plumes can not be penetrated by optical remote sensing techniques. One option to overcome this difficulty could be in situ and remote sensing measurements from drones flying into volcanic plumes. At least close to the edge of the plume, the aerosol extinction might be retrieved from dirct sun measurements.

b) What is the consequence of 3D effects for the quantification of emission fluxes from real volcanoes? The simulations of

660   this study were made for idealised volcanic plumes. In reality, more complex plume configurations will occur. Thus in particular two scenarios should be investigated: 1) confined or vertical plumes: in many cases (for small plumes) enhanced trace gas absorptions are found only directly above the volcano or close to it. If the horizontal wind speeds are low, also a vertically oriented plume might contribute to the observed trace gas absorption. 2) horizontal plumes: for larger eruptions often elongated plumes are found, which are dominated by horizontal transport. Both scenarios should be simulated and

665   eventually a direct connection between the observed trace gas SCDs and the emission flux from the volcano should be established. Such simulations will be carried out in a follow-up study.

c) How important are 3D effects for other confined trace gas plumes? Confined trace gas plumes also occur for other localised emission sources, in particular power plants. For measurements of the SO_2 emissions from power plants (in the UV spectral range), a similar strong underestimation will occur (up to more than 50%) as for the volcanic plumes. As shown in

670   this study, for NO_2 observations in the blue spectral range the light mixing effect is much smaller than for the UV spectral range. But these results were obtained for a pure Rayleigh atmosphere outside the plume. Since power plant emissions usually occur in polluted regions with high aerosol concentrations, aerosol scattering will enhance the diffuse atmospheric radiation compared to a pure Rayleigh atmosphere, which will possibly increase the light mixing. Also 3D effects for realistic power plant plumes will be addressed in a forthcoming study.

675

Author contributions

TW performed the simulations and prepared the manuscript with contributions from all co-authors.

685 **Competing interests**

Thomas Wagner is executive editor of AMT.

References
690

Afe, O. T., Richter, A., Sierk, B., Wittrock, F., and Burrows, J. P.: BrO emissions from volcanoes: a survey using GOME and SCIAMACHY measurements, Geophys. Res. Lett., 31, L24113, https://doi.org/10.1029/2004GL020994, 2004.

Bazalgette Courrèges-Lacoste, G., M. Sallusti, G. Bulsa, G. Bagnasco, Ben Veihelmann, S. Riedl, D. J. Smith, R. Maurer, "The Copernicus Sentinel 4 mission: a geostationary imaging UVN spectrometer for air quality monitoring," Proc. SPIE

695 10423, Sensors, Systems, and Next-Generation Satellites XXI, 1042307 (29 September 2017); https://doi.org/10.1117/12.2282158

Bobrowski, N., Hönninger, G., Galle, B., Platt, U., Detection of bromine monoxide in a volcanic plume. Nature 423, 273–276, 2003.

Bobrowski, N., U. Platt, SO_2/BrO ratios studied in five volcanic plumes, Journal of Volcanology and Geothermal Research,

700 Volume 166, Issues 3–4, Pages 147-160, 2007.

Bobrowski, N., Kern, C., Platt, U., Hörmann, C., and Wagner, T.: Novel SO2 spectral evaluation scheme using the 360–390 nm wavelength range, Atmos. Meas. Tech., 3, 879-891, doi:10.5194/amt-3-879-2010, 2010.

Bobrowski, N. and Giuffrida, G.: Bromine monoxide / sulphur dioxide ratios in relation to volcanological observations at Mt. Etna 2006–2009, Solid Earth, 3, 433–445, https://doi.org/10.5194/se-3-433-2012, 2012.

705 Bogumil, K., J. Orphal, J. P. Burrows, Temperature dependent absorption cross sections of O3, NO2, and other atmospheric trace gases measured with the SCIAMACHY spectrometer, Proc. ERS - Envisat Symposium. Looking down at our Earth in the New Millennium, Gothenburg 16 - 20 October 2000.

Bovensmann, H., J. P. Burrows, M. Buchwitz, J. Frerik, S. Noël, V. V. Rozanov, K. V. Chance, and A. Goede (1999), SCIAMACHY—Mission objectives and measurement modes, J. Atmos. Sci., 56, 127–150.

710 Burrows, J. P., et al. (1999), The Global Ozone Monitoring Experiment (GOME): Mission concept and first scientific results, J. Atmos. Sci., 56, 151–175.

Callies, J., Corpaccioli, E., Eisinger, M., Hahne, A., and Lefebvre, A.: GOME-2 – MetOp's second-generation sensor for operational ozone monitoring, ESA Bull., 102, 28–36, 2000.

Dinger, F., Kleinbek, T., Dörner, S., Bobrowski, N., Platt, U., Wagner, T., Ibarra, M., and Espinoza, E.: SO2 and BrO

715 emissions of Masaya volcano from 2014 to 2020, Atmos. Chem. Phys., 21, 9367–9404, https://doi.org/10.5194/acp-21-9367-2021, 2021.

Eisinger, M. and Burrows, J. P.: Tropospheric sulfur dioxide observed by the ERS-2 GOME instrument, Geophys. Res. Lett., 25, 4177–4180, 1998.

Fioletov, V. E., McLinden, C. A., Krotkov, N., Li, C., Joiner, J., Theys, N., Carn, S., and Moran, M. D.: A global catalogue

720 of large SO_2 sources and emissions derived from the Ozone Monitoring Instrument, Atmos. Chem. Phys., 16, 11497–11519, https://doi.org/10.5194/acp-16-11497-2016, 2016.

Flynn, L. E., Seftor, C. J., Larsen, J. C., and Xu, P.: The Ozone Mapping and Profiler Suite, in: Earth Science Satellite Remote Sensing, edited by: Qu, J. J., Gao,W., Kafatos, M., Murphy, R. E., and Salomonson, V. V., Springer, Berlin, 279–296, doi:10.1007/978-3-540-37293-6, 2006.

725 Heue, K.-P., Brenninkmeijer, C. A. M., Baker, A. K., Rauthe-Schöch, A., Walter, D., Wagner, T., Hörmann, C., Sihler, H., Dix, B., Frieß, U., Platt, U., Martinsson, B. G., van Velthoven, P. F. J., Zahn, A., and Ebinghaus, R.: SO_2 and BrO observation in the plume of the Eyjafjallajökull volcano 2010: CARIBIC and GOME-2 retrievals, Atmos. Chem. Phys., 11, 2973–2989, https://doi.org/10.5194/acp-11-2973-2011, 2011.

Atmospheric
Measurement
Techniques
Discussions

Hönninger, G., Referenzspektren reaktiver Halogenverbindungen für DOAS-Messungen, Diploma thesis, Univ. of
730   Heidelberg, Heidelberg, Germany, 1999.

Hörmann, C., Sihler, H., Bobrowski, N., Beirle, S., Penning de Vries, M., Platt, U., and Wagner, T.: Systematic investigation
of bromine monoxide in volcanic plumes from space by using the GOME-2 instrument, Atmos. Chem. Phys., 13, 4749–
4781, https://doi.org/10.5194/acp-13-4749-2013, 2013.

Kern, C., T. Deutschmann, L. Vogel, M. Wöhrbach, T. Wagner and U. Platt, Radiative transfer corrections for accurate
735   spectroscopic measurements of volcanic gas emissions. Bull Volcanol 72, 233–247 (2010). https://doi.org/10.1007/s00445-
009-0313-7.

Kern, C., A.H. Lerner, T. Elias, P. Nadeau, P.J. Kelly, C.A. Werner, L.E. Chlor, M. Cappos, Quantifying gas emissions
associated with the 2018 rift eruption of Kīlauea Volcano using ground-based DOAS measurements. *Bull Volcanol* **82,** 55
(2020).

740   Khokhar, M. F., Frankenberg, C., Van Roozendael, M., Beirle, S., Kühl, S., Richter, A., Platt, U., and Wagner, T.: Satellite
Observations of Atmospheric SO2 from Volcanic Eruptions during the Time Period of 1996 to 2002, J. Adv. Space Res., 36,
879–887, https://doi.org/10.1016/j.asr.2005.04.114, 2005.

Krotkov, N. A., Carn, S. A., Krueger, A. J., Bhartia, P. K., and Yang, K.: Band residual difference algorithm for retrieval of
SO_2 from the Aura Ozone Monitoring Instrument (OMI), IEEE T. Geosci. Remote Sens., AURA Special Issue, 44, 1259–
745   1266, https://doi.org/10.1109/TGRS.2005.861932, 2006.

Krueger, A. J.: Sighting of El Chichon sulfur dioxide clouds with the Nimbus 7 total ozone mapping spectrometer, Science,
220, 1377–1379, 1983.

Levelt, P. F., van den Oord, G. H. J., Dobber, M. R., Malkki, A.,

Visser, H., de Vries, J., Stammes, P., Lundell, J. O. V., and Saari, H.: The Ozone Monitoring Instrument, IEEE T. Geosci.
750   Remote, 44, 1093–1101, https://doi.org/10.1109/TGRS.2006.872333, 2006.

Li, C., Joiner, J., Krotkov, N. A., and Bhartia, P. K.: A fast and sensitive new satellite SO2 retrievalalgorithm based on
principal component analysis: Application to the ozone monitoring instrument, Geophys. Res. Lett., 40, 6314–6318,
https://doi.org/10.1002/2013GL058134, 2013.

Lyapustin, A. and Kaufman, Y., Role of adjacency effect in the remote sensing of aerosol, J. Geophys. Res. Atmos., 106,
755   11909–11916, https://doi.org/10.1029/2000JD900647, 2001.

Marquard, L.C., T. Wagner, and U. Platt, Improved Air Mass Factor Concepts for Scattered Radiation Differential Optical
Absorption Spectroscopy of Atmospheric Species, *J. Geophys. Res.,105, 1315-1327, 2000* .

Nowlan, C. R., Liu, X., Chance, K., Cai, Z., Kurosu, T. P., Lee, C., and Martin, R. V.: Retrievals of sulfur dioxide from the
Global Ozone Monitoring Experiment 2 (GOME-2) using an optimal estimation approach: Algorithm and initial validation,
760   J. Geophys. Res., 116, D18301, https://doi.org/10.1029/2011JD015808, 2011.

Penning de Vries, M. J. M., Dörner, S., Puķīte, J., Hörmann, C., Fromm, M. D., and Wagner, T.: Characterisation of a
stratospheric sulfate plume from the Nabro volcano using a combination of passive satellite measurements in nadir and limb
geometry, Atmos. Chem. Phys., 14, 8149–8163, https://doi.org/10.5194/acp-14-8149-2014, 2014.

Puķīte, J., Kühl, S., Deutschmann, T., Platt, U., and Wagner, T.: Extending differential optical absorption spectroscopy for
765   limb measurements in the UV, Atmos. Meas. Tech., 3, 631–653, https://doi.org/10.5194/amt-3-631-2010, 2010.

Puķīte, J. and Wagner, T.: Quantification and parametrization of non-linearity effects by higher-order sensitivity terms in
scattered light differential optical absorption spectroscopy, Atmos. Meas. Tech., 9, 2147-2177, doi:10.5194/amt-9-2147-
2016, 2016.

Richter, R., A fast atmospheric correction algorithm applied to Landsat TM images, Remote Sens., 11, 159–166,
770   https://doi.org/10.1080/01431169008955008, 1990.

Rix, M., Valks, P., Hao, N., Loyola, D. G., Schlager, H., Huntrieser, H. H., Flemming, J., Koehler, U., Schumann, U., and Inness, A.: Volcanic SO2, BrO and plume height estimations using GOME-2 satellite measurements during the eruption of Eyjafjallajökull in May 2010, J. Geophys. Res., 117, D00U19, https://doi.org/10.1029/2011JD016718, 2012.

775 Rothman, L. S., Jacquemart, D., Barbe, A., Benner, D. C., Birk, M., Brown, L. R., Carleer, M. R., Chackerian Jr., C., Chance, K., Coudert, L. H., Dana, V., Devi, V. M., Flaud, J.-M., Gamache, R. R., Goldman, A., Hartmann, J.-M., Jucks, K. W., Maki, A.

Mandin, G., J.-Y., Massie, S. T., Orphal, J., Perrin, A., Rinsland, C. P., Smith, M. A. H., Tennyson, J., Tolchenov, R. N., Toth, R. A., Vander Auwera, J., Varanasi, P., and Wagner, G.: The HITRAN 2004 molecular spectroscopic database, J. Quant. Spectrosc. Ra., 96, 139–204, 2005.

780 Schönhardt, A., Richter, A., Theys, N., and Burrows, J. P.: Space-based observation of volcanic iodine monoxide, Atmos. Chem. Phys., 17, 4857–4870, https://doi.org/10.5194/acp-17-4857-2017, 2017.

Schwaerzel, M., Emde, C., Brunner, D., Morales, R., Wagner, T., Berne, A., Buchmann, B., and Kuhlmann, G., Three-dimensional radiative transfer effects on airborne and ground-based trace gas remote sensing, Atmos. Meas. Tech., 13, 4277–4293, https://doi.org/10.5194/amt-13-4277-2020, 2020.

785 Schwaerzel, M., Brunner, D., Jakub, F., Emde, C., Buchmann, B., Berne, A., and Kuhlmann, G.: Impact of 3D radiative transfer on airborne NO2 imaging remote sensing over cities with buildings, Atmos. Meas. Tech., 14, 6469–6482, https://doi.org/10.5194/amt-14-6469-2021, 2021.

Suleiman, R. M., Chance, K., Liu, X., González Abad, G., Kurosu, T. P., Hendrick, F., and Theys, N.: OMI total bromine monoxide (OMBRO) data product: algorithm, retrieval and measurement comparisons, Atmos. Meas. Tech., 12, 2067–2084,
790 https://doi.org/10.5194/amt-12-2067-2019, 2019.

Theys, N., Van Roozendael, M., Dils, B., Hendrick, F., Hao, N., and De Mazière, M. (2009), First satellite detection of volcanic bromine monoxide emission after the Kasatochi eruption, Geophys. Res. Lett., 36, L03809, doi:10.1029/2008GL036552.

Theys, N., De Smedt, I., Van Roozendael, M., Froidevaux, L., Clarisse, L., and Hendrick, F., First satellite detection of
795 volcanic OClO after the eruption of Puyehue-Cordón Caulle, Geophys. Res. Lett., 41, 667– 672, doi:10.1002/2013GL058416, 2014.

Theys, N., De Smedt, I., van Gent, J., Danckaert, T., Wang, T., Hendrick, F., Stavrakou, T., Bauduin, S., Clarisse, L., Li, C., Krotkov, N. A., Yu, H., Van Roozendael, M.: Sulfur dioxide vertical column DOAS retrievals from the Ozone Monitoring Instrument: Global observations and comparison to ground-based and satellite data, J. Geophys. Res.-Atmos., 120, 2470–
800 2491, https://doi.org/10.1002/2014JD022657, 2015.

Theys, N., De Smedt, I, Yu, H., Danckaert, T., van Gent, J., Hörmann, C., Wagner, T., Hedelt, P., Bauer, H., Romahn, F., Pedergnana, M., Loyola, D., and Van Roozendael, M.: Sulfur dioxide retrievals from TROPOMI onboard Sentinel-5 Precursor: algorithm theoretical basis, Atmos. Meas. Tech., 10, 119–153, https://doi.org/10.5194/amt-10-119-2017, 2017.

Theys, N., Hedelt, P., Smedt, I. De, Lerot, C., Yu, H., Vlietinck, J., Pedergnana, M., Arellano, S., Galle, B., Fernandez, D.,
805 Barrington, C., Taine, B., Loyola, D., and Van Roozendael, M.: Global monitoring of volcanic SO2 degassing from space with unprecedented resolution, Nature Scientific Reports, 9, 2643, https://doi.org/10.1038/s41598-019-39279-y, 2019.

Theys, N., Hedelt, P., Smedt, I. De, Lerot, C., Yu, H., Vlietinck, J., Pedergnana, M., Arellano, S., Galle, B., Fernandez, D., Barrington, C., Taine, B., Loyola, D., and Van Roozendael, M.: Global monitoring of volcanic SO_2 degassing from space with unprecedented resolution, Nature Scientific Reports, 9, 2643, https://doi.org/10.1038/s41598-019-39279-y, 2019.

810 Theys, N., Fioletov, V., Li, C., De Smedt, I., Lerot, C., McLinden, C., Krotkov, N., Griffin, D., Clarisse, L., Hedelt, P., Loyola, D., Wagner, T., Kumar, V., Innes, A., Ribas, R., Hendrick, F., Vlietinck, J., Brenot, H., and Van Roozendael, M.: A sulfur dioxide Covariance-Based Retrieval Algorithm (COBRA): application to TROPOMI reveals new emission sources, Atmos. Chem. Phys., 21, 16727–16744, https://doi.org/10.5194/acp-21-16727-2021, 2021a.

Theys, N., I. De Smedt, C. Lerot, H. Yu, M. Van Roozendael, S5P/TROPOMI SO2ATBD, Doc. No.: S5P-BIRA-L2-ATBD-
400E, Issue 2.3.0, https://sentinels.copernicus.eu/documents/247904/2476257/Sentinel-5P-ATBD-SO2-TROPOMI, 2021b.

United States Committee on Extension to the Standard Atmosphere: U.S. Standard Atmosphere, 1976, National Oceanic and
Atmospheric Administration, National Aeronautics and Space Administration, United States Air Force, Washington D.C.,
1976.

Vandaele, A. C., Hermans, C., Simon, P. C., Carleer, M., Colin, R., Fally, S., Mérienne, M.-F., Jenouvrier, A., and Coquart,
B.: Measurements of the NO2 Absorption Cross-section from 42000 cm−1 to 10000 cm−1 (238–1000 nm) at 220K and 294
K, J. Quant. Spectrosc. Ra., 59, 171–184, 1997.

Veefkind, J., Aben, I., McMullan, K., Förster, H., de Vries, J., Otter, G., Claas, J., Eskes, H., de Haan, J., Kleipool, Q., van
Weele, M., Hasekamp, O., Hoogeveen, R., Landgraf, J., Snel, R., Tol, P., Ingmann, P., Voors, R., Kruizinga, B., Vink, R.,
Visser, H., and Levelt, P.: TROPOMI on the ESA Sentinel-5 Precursor: A GMES mission for global observations of the
atmospheric composition for climate, air quality and ozone layer applications, Remote Sens. Environ., 120, 70–83,
https://doi.org/10.1016/j.rse.2011.09.027, 2012.

Wagner, T., J. P. Burrows, T. Deutschmann, B. Dix, C. von Friedeburg, U. Frieß, F. Hendrick, K.-P. Heue, H. Irie, H.
Iwabuchi, Y. Kanaya, J. Keller, C. A. McLinden, H. Oetjen, E. Palazzi, A. Petritoli, U. Platt, O. Postylyakov, J. Pukite, A.
Richter, M. van Roozendael, A. Rozanov, V. Rozanov, R. Sinreich, S. Sanghavi, F. Wittrock, Comparison of Box-Air-Mass-
Factors and Radiances for Multiple-Axis Differential Optical Absorption Spectroscopy (MAX-DOAS) Geometries
calculated from different UV/visible Radiative Transfer Models, Atmos. Chem. Phys., 7, 1809-1833, 2007.

Warnach, S., Bromine monoxide in volcanic plumes - A global survey of volcanic plume composition and chemistry derived
from Sentinel-5 Precursor/TROPOMI data, PhD thesis, University of Heidelberg, 2022.

Wilmouth, D. M., Hanisco, T. F., Donahue, N. M., and Anderson, J. G.: Fourier Transform Ultraviolet Spectroscopy of the
A 2P3/2–X 2P3/2 Transition of BrO, J. Phys. Chem. A, 103, 8935–8945, doi:10.1021/jp991651o, 1999.

Yang, K., Krotkov, N., Krueger, A., Carn, S., Bhartia, P. K., and Levelt, P.: Retrieval of Large Volcanic SO2 columns from
the Aura Ozone Monitoring Instrument (OMI): Comparisons and Limitations, J. Geophys. Res., 112, D24S43,
https://doi.org/10.1029/2007JD008825, 2007.

Yang, K., Liu, X., Bhartia, P., Krotkov, N., Carn, S., Hughes, E., Krueger, A., Spurr, R., and Trahan, S.: Direct retrieval of
sulfur dioxide amount and altitude from spaceborne hyperspectral UV measurements: Theory and application, J. Geophys.
Res., 115, D00L09, https://doi.org/10.1029/2010JD013982, 2010.

Zhang, Y., Li, C., Krotkov, N. A., Joiner, J., Fioletov, V., and McLinden, C.: Continuation of long-term global SO2
pollution monitoring from OMI to OMPS, Atmos. Meas. Tech., 10, 1495–1509, https://doi.org/10.5194/amt-10-1495-2017,
2017.

Tables

865

Table 1: Ground pixel sizes* and expected SO$_2$ SCDs for an SO$_2$ plume with a horizontal extension smaller than a TROPOMI pixel and a SO$_2$ SCD of $1 \cdot 10^{16}$ molec/cm² (close to the detection limit) for a GOME-2 observation.

Instrument	Pixel size [km x km]	Area [km²]	SO$_2$ SCD [molec/cm²]	SCD ratio with respect to the GOME-2 SCD
GOME-1 (Burrows et al., 1999)	40 x 320	12800	$2.5 \cdot 10^{15}$	0.25
GOME-2 (Callies et al., 2000)	40 x 80	3200	$1 \cdot 10^{16}$	1
OMPS (Flynn et al., 2006)	50 x 50	2500	$1.28 \cdot 10^{16}$	1.28
SCIAMACHY (Bovensmann et al., 1999)	30 x 60	1800	$1.78 \cdot 10^{16}$	1.78
OMI (Levelt et al., 2006)	13 x 23	299	$1.07 \cdot 10^{17}$	10.7
TROPOMI (Veefkind et al., 2021)	3.5 x 5.5	19.25	$1.66 \cdot 10^{18}$	166.2

*for OMI and TROPOMI at nadir

870

Table 2: Free horizontal light paths (e-folding lengths) for different wavelengths and altitudes considering only Rayleigh scattering.

Altitude	light path length at 313 nm (km)	light path length at 350 nm (km)	light path length at 440 nm (km)
0-1 km	9	16	30
5-6 km	14	25	47
10-11 km	35	66	122

875

Table 3: Plume extensions and corresponding trace gas VCDs and AODs used in this study. For a given scenario the amount of trace gas is assumed to be constant but is distributed over different plume volumes (depending on the horizontal plume extension). The trace gas VCDs of the scenarios with 1 x 1 km² horizontal extension is used to identify the corresponding scenario in this study.

Scenario	Trace gas VCDs for different horizontal plume extension								
	1 km	2 km	4 km	6 km	10 km	14 km	20 km	30 km	40 km
BrO VCD ($1 \cdot 10^{13}$molec/cm²)	100	25	6.25	2.78	1	0.51	0.25	0.11	0.06
IO VCD ($1 \cdot 10^{13}$molec/cm²)	500	125	31.3	13.9	5	2.55	1.25	0.56	0.31
SO$_2$ VCD$_{weak}$ ($1 \cdot 10^{17}$molec/cm²)	4	1	0.25	0.11	0.04	0.02	0.01	0.004	0.003
SO$_2$ VCD$_{strong, 1}$ ($1 \cdot 10^{17}$molec/cm²)	100	25	6.25	2.78	1	0.51	0.25	0.11	0.06
SO$_2$ VCD$_{strong, 2}$ ($1 \cdot 10^{17}$molec/cm²)	250	62.5	15.6	6.9	2.5	1.28	0.63	0.28	0.16
SO$_2$ VCD$_{strong, 3}$ ($1 \cdot 10^{17}$molec/cm²)	1000	250	62.5	27.8	10	5.10	2.50	1.11	0.63
SO$_2$ VCD$_{strong, 4}$ ($1 \cdot 10^{17}$molec/cm²)	4000	1000	250	111	40	20.4	10	4.44	2.5
Aerosol AOD	10	2.5	0.625	0.278	0.1	0.051	0.025	0.011	0.006

Atmospheric
Measurement
Techniques
Open Access
Discussions

EGU

Table 4: SO$_2$ VCDs (for a 1 x 1 x 1 km³ plume), chosen wavelengths, absorption cross sections and corresponding
880 **vertical optical depths for the strong SO$_2$ scenarios (see table 3).**

Wavelength / Absorption cross section	SO$_2$ VCD$_{strong, 1}$ $1 \cdot 10^{19}$ molec/cm²	SO$_2$ VCD$_{strong, 2}$ $2.5 \cdot 10^{19}$ molec/cm²	SO$_2$ VCD$_{strong, 3}$ $1 \cdot 10^{20}$ molec/cm²	SO$_2$ VCD$_{strong, 4}$ $4 \cdot 10^{20}$ molec/cm²
313.1 nm / $2.45 \cdot 10^{-19}$ cm²	2.45	6.13	24.5	98
324.15 nm / $1.55 \cdot 10^{-20}$ cm²	0.16	0.39	1.55	6.2
332.0 nm / $1 \cdot 10^{-21}$ cm²	0.01	0.025	0.1	0.4
370.3 nm / $6 \cdot 10^{-22}$ cm²	0.006	0.015	0.06	0.24

885 **Figures**
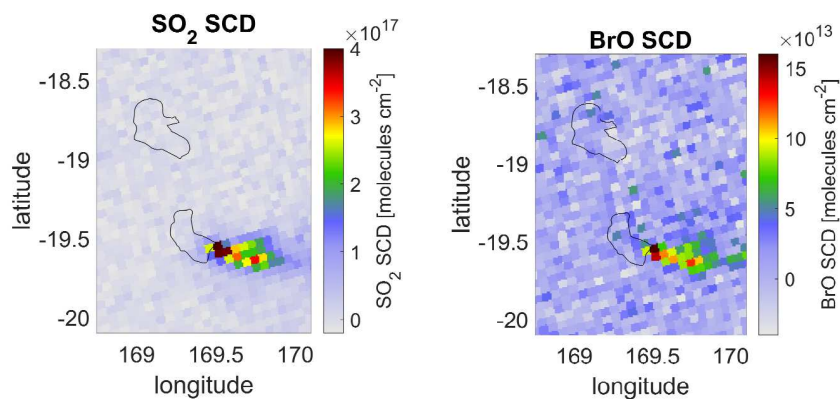
Fig. 1: TROPOMI observations of the plume of Mount Yasur on 24.06.2020 (Warnach, 2022).

890

895

900

905
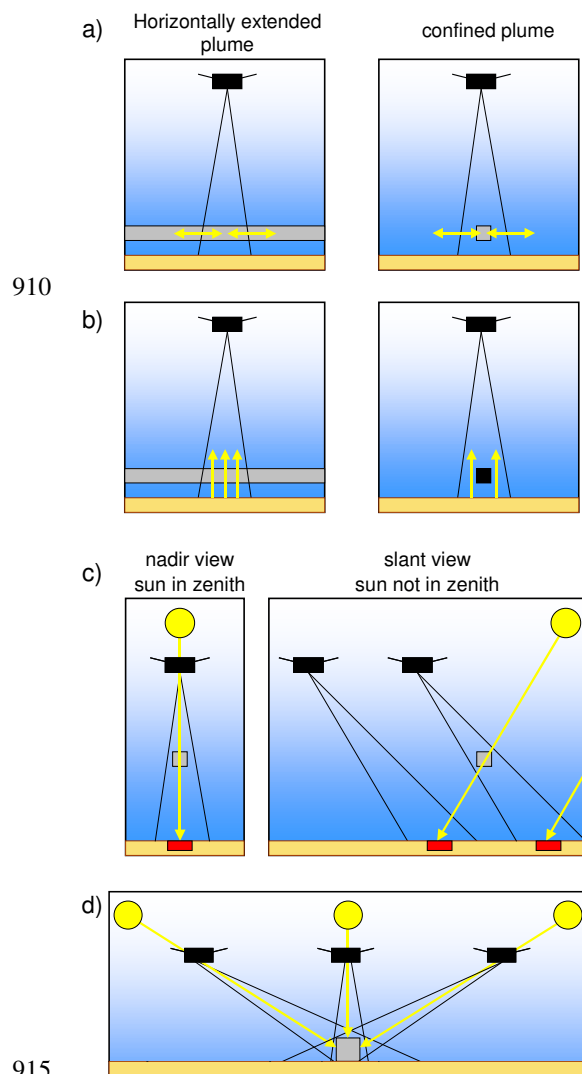
Fig. 2: The four 3D effects investigated in this study. a) Light mixing effect: part of the light seen by the satellite sensor originates from outside the satellite ground pixel. For horizontally confined plumes (right), such light paths contain no trace gas absorption. b) Saturation effect: for strongly absorbing species like SO_2, the incoming sun light might be almost fully absorbed in the plume. This can lead to a strong underestimation for narrow plumes with high trace gas concentration. c) geometric effect: depending on the illumination and viewing geometry, the location of the ground pixel with enhanced trace gas absorption (the projection of the plume along the direction of the incoming sun light, red marks at the surface) can systematically differ from the true plume location (grey square). d) Plume side effect: for narrow volcanic plumes the contributions of photons reaching the sensor from the sides of the plume becomes important.
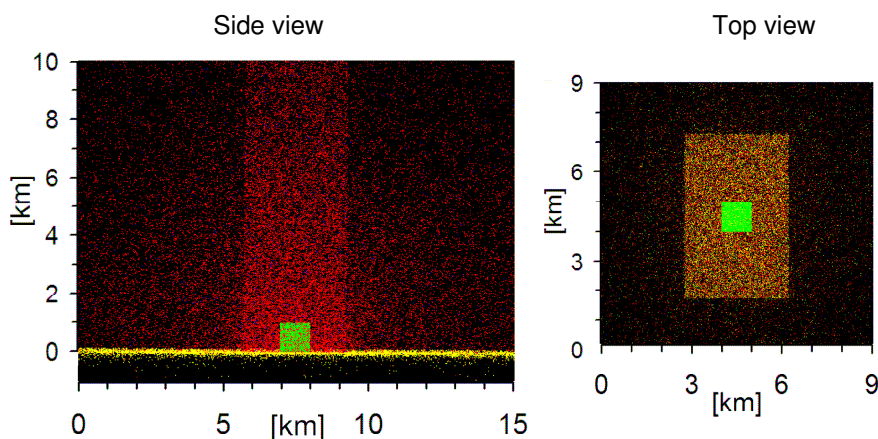
Fig. 3: Exemplary simulation results from the Monte Carlo radiative transfer model TRACY-2. An idealised narrow volcanic plume (1 x 1 x 1 km³) is observed by TROPOMI with a FOV according to a ground pixel size of 3.5 x 5.5 km². Red dots indicate Rayleigh scattering events, yellow dots surface reflections, and green dots aerosol scattering events (the volcanic plume is filled with purely scattering aerosols). Simulations are performed for 340 nm with 25000 photons for overhead sun and a nadir-looking satellite instrument.
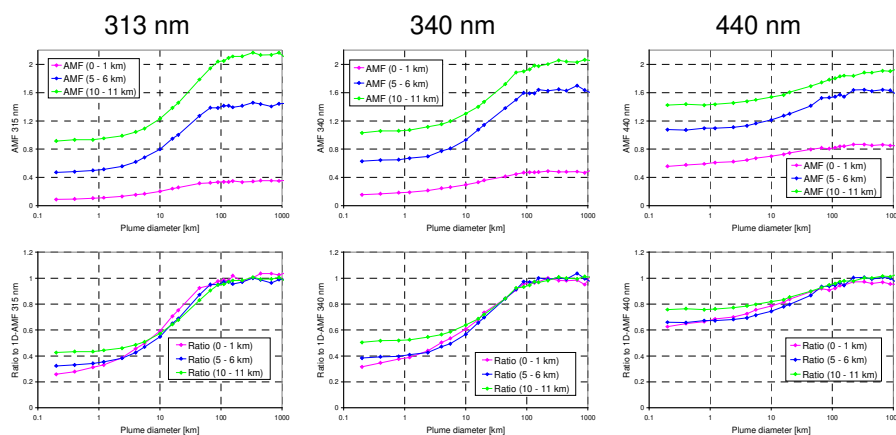
Fig. 4: Dependence of the AMF on the horizontal plume extension. Top: AMFs for different plume altitudes and wavelengths; bottom: AMFs normalised by the corresponding 1D AMFs (assuming a horizontally extended plume. The simulations are performed for SZA: 0°, VZA: FOV: 0.014°, satellite altitude: 824 km asl, no aerosols.
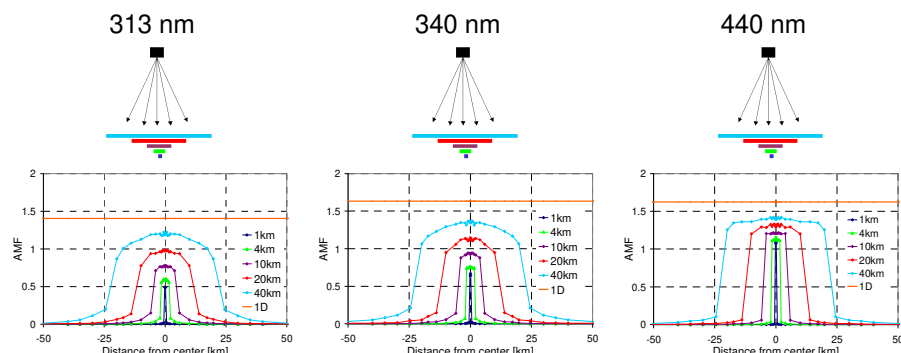
Fig. 5 AMFs for plume scans in near-nadir viewing geometry (SZA=0°, VZA=0°) at different wavelengths. It is assumed that the satellite scans the plume with a narrow FOV (~ 0.014°). The different colours represent AMFs for plumes at 5-6 km altitude and with different horizontal extensions (from 1 x 1 km² to 40 x 40 km²).

960
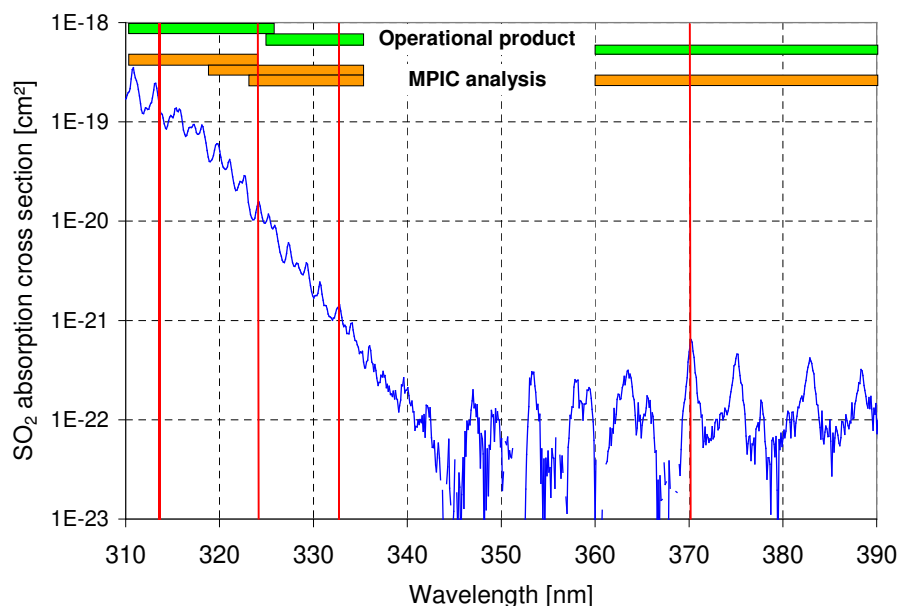
Fig. 6 SO₂ absorption cross section (273K, Bogumil et al., 2000, see also https://www.iup.uni-remen.de/gruppen/molspec/databases/sciamachydata/index.html). The green and orange bars indicate different SO₂ fit ranges used in the operational TROPOMI product and the MPIC SO₂ retrieval. The vertical bars indicate wavelengths used in the 3D RTM simulations.

965

970

975
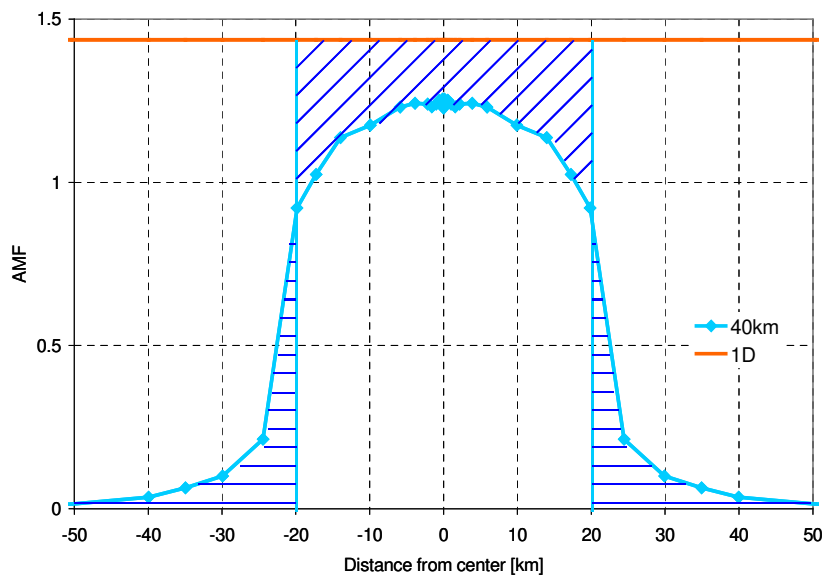
980

Fig. 7 AMFs for plume scans (as in Fig. 4) in near-nadir viewing geometry (SZA=0°) for 313 nm and a plume at 5-6 km altitude. In the area of the plume the AMFs are smaller than the 1D-AMF, whereas outside they are larger than zero. The differences are indicated by the blue marked areas for a plume of 40 x 40 km².

985

990

995

1000

1005

1010

Atmospheric
Measurement
Techniques
Open Access
EGU
Discussions

Ground pixel size: 3.5 x 5.5 km² (TROPOMI)

Ground pixel size: 200 x 200 km²
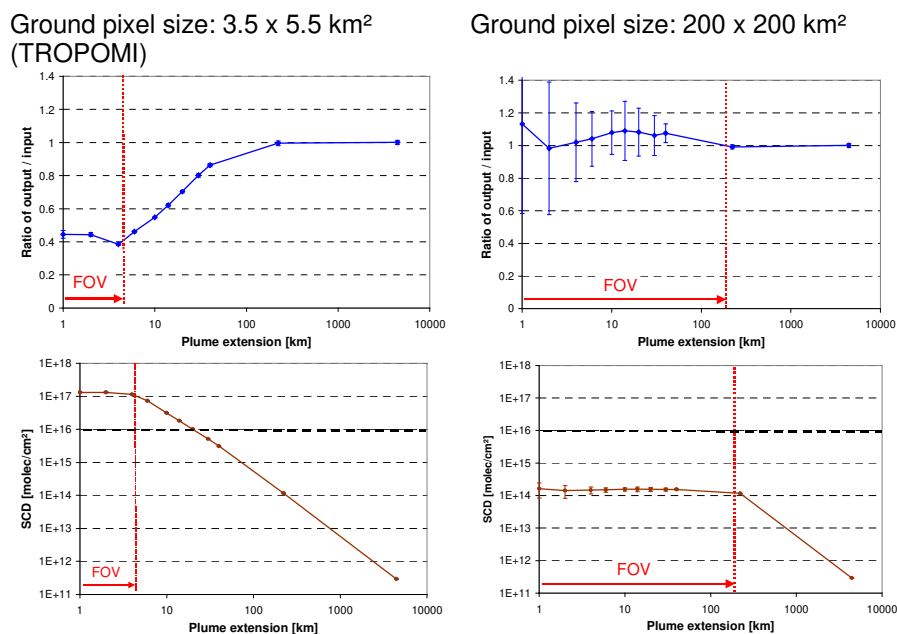
Fig. 8 Top: Fraction of molecules that is detected inside a ground pixel (using a 1D-AMF) as a function of the horizontal plume extension (note the logarithmic scale) for measurements at 313 nm. Bottom: measured SO$_2$ for a SO$_2$ VCD (for a 1 x 1 km² pixel) of $1 \cdot 10^{18}$ molec/cm². The horizontal dashed line indicates the detection limit (assuming an OD threshold of 0.001). Left: results for a TROPOMI ground pixel; right: results for a large ground pixel of 200 x 200 km². Note that in the case of plume size > ground pixel size, only the fraction of the plume within the ground pixel size is considered. Simulations for a plume altitude from 5 to 6 km, wavelength of 313 nm and for VZA=0, and SZA=0°.

Atmospheric
Measurement
Techniques
Discussions

313 nm

0.9%	1.5%	2.1%	1.5%	0.9%
<0.001	<0.001	<0.001	<0.001	<0.001
1.3%	3.2%	43.6%	3.2%	1.3%
		▨		
<0.001	<0.001	0.003	<0.001	<0.001
0.9%	1.5%	2.1%	1.5%	0.9%
<0.001	<0.001	<0.001	<0.001	<0.001

340 nm

0.6%	1.3%	1.9%	1.3%	0.6%
<0.0005	<0.0005	<0.0005	<0.0005	<0.0005
1.1%	2.8%	47.1%	2.8%	1.1%
		▨		
<0.0005	<0.0005	0.004	<0.0005	<0.0005
0.6%	1.3%	1.9%	1.3%	0.6%
<0.0005	<0.0005	<0.0005	<0.0005	<0.0005

440 nm

0.3%	0.6%	0.7%	0.6%	0.3%
<0.0005	<0.0005	<0.0005	<0.0005	<0.0005
0.4%	1.4%	71.3%	1.4%	0.4%
		▨		
<0.0005	<0.0005	0.006	<0.0005	<0.0005
0.3%	0.6%	0.7%	0.6%	0.3%
<0.0005	<0.0005	<0.0005	<0.0005	<0.0005

Fig. 9 Horizontal coverage of a 1 x 1 x 1 km³ plume (yellow hatched areas) by TROPOMI observations at different wavelengths. The numbers at the top of the TROPOMI pixels indicate the fractions of the plume molecules retrieved from that ground pixel. The numbers at the bottom indicate the optical depth of the trace gas absorption. Red values represent results above the respective detection limit
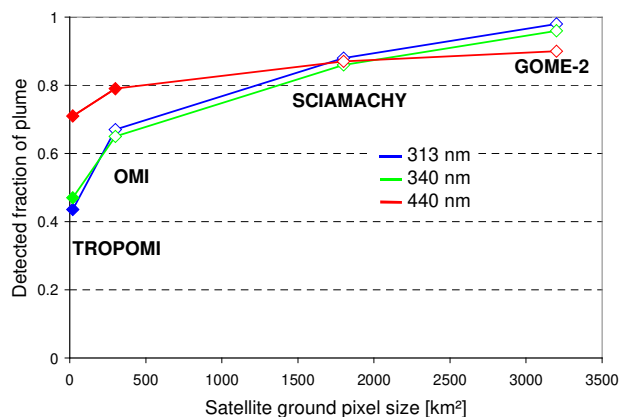
Fig. 10 Fraction of the plume content detected for different satellite sensors if a 1D-AMF is applied (for a 1 x 1 x 1 km³ plume at 5 – 6 km altitude). Full symbols indicate observations above the detection limit.

Atmospheric
Measurement
Techniques
Discussions
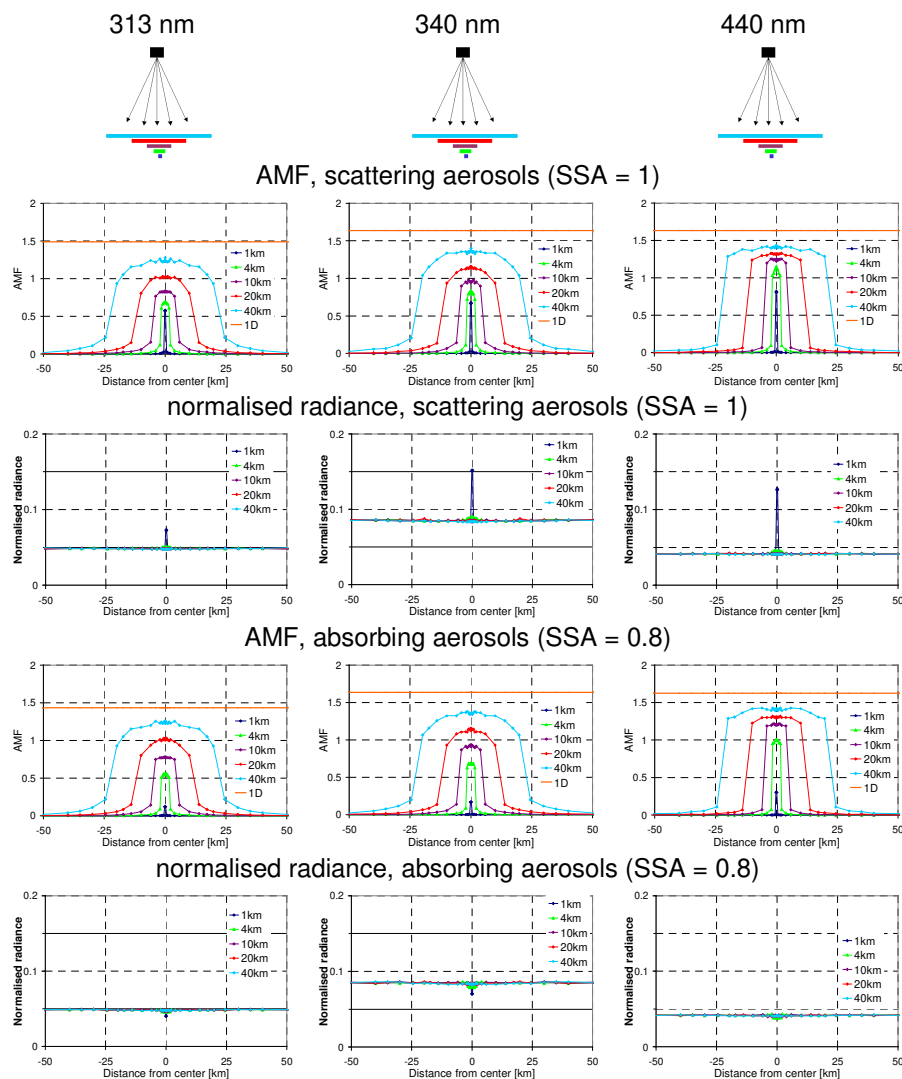
1070 **Fig. 11 AMFs and normalised radiances for plume scans in near-nadir viewing geometry (SZA=0°) for different wavelengths and aerosol contents. The satellite scans the plume with a narrow FOV (~ 0.014°). The different colours represent AMFs for plumes at 5 – 6 km altitude and with different horizontal extensions (from 1 x 1 km² to 40 x 40 km²). The rather low radiance at 313 nm (in spite of the high probability of Rayleigh scattering) is caused by the stratospheric ozone absorption.**

1075

1080

1085

A) 5 – 6 km

B) 0 – 1 km
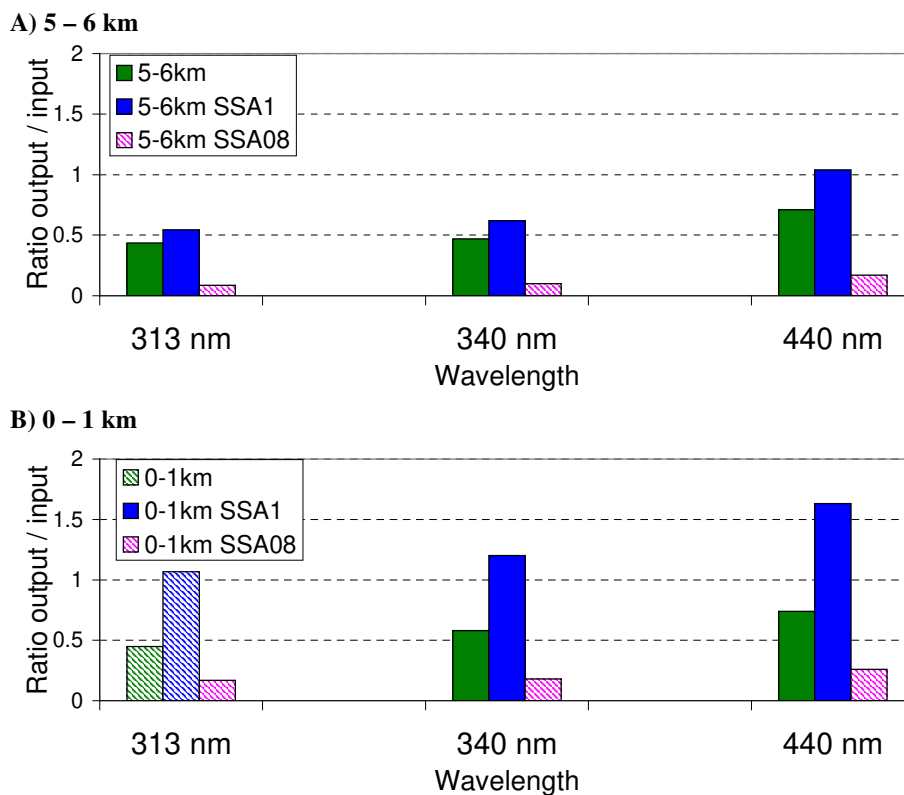
Fig. 12 Fraction of the plume content detected for different plume heights and aerosol scenarios if the respective 1D-AMF at 0 – 1 km or 5 – 6 km altitude (without aerosols) is applied for TROPOMI observations (horizontal plume extension 1 x 1 km²). Hatched bars indicate scenarios, for which the absorption is below the detection limit for the trace gas scenarios described in section 2.1 (results for the satellite pixel directly above the plume).
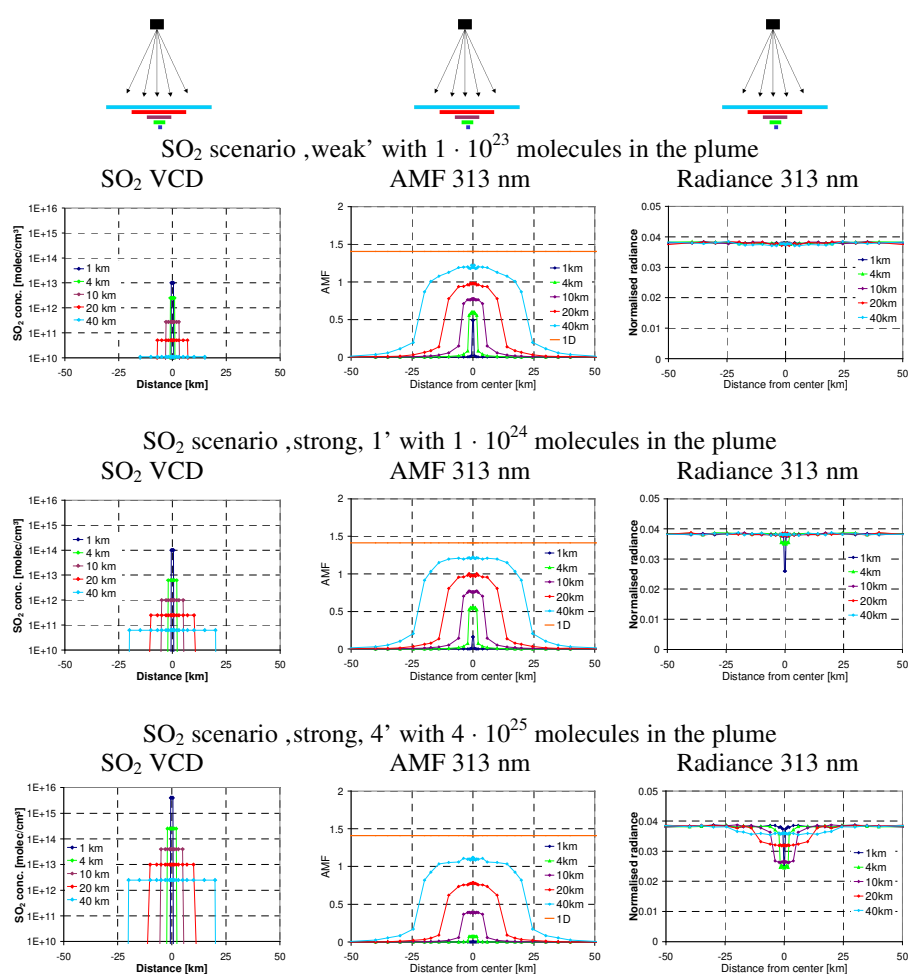
Fig. 13 Plume scan for SO₂ plumes with different amounts of molecules and different horizontal extensions (for the different SO₂ scenarios, see table 3). Left: SO₂ VCDs of the plumes, middle: AMFs at 313 nm; right: normalised radiance at 313 nm.

1120

1125

1130

1135

Atmospheric
Measurement
Techniques
Discussions
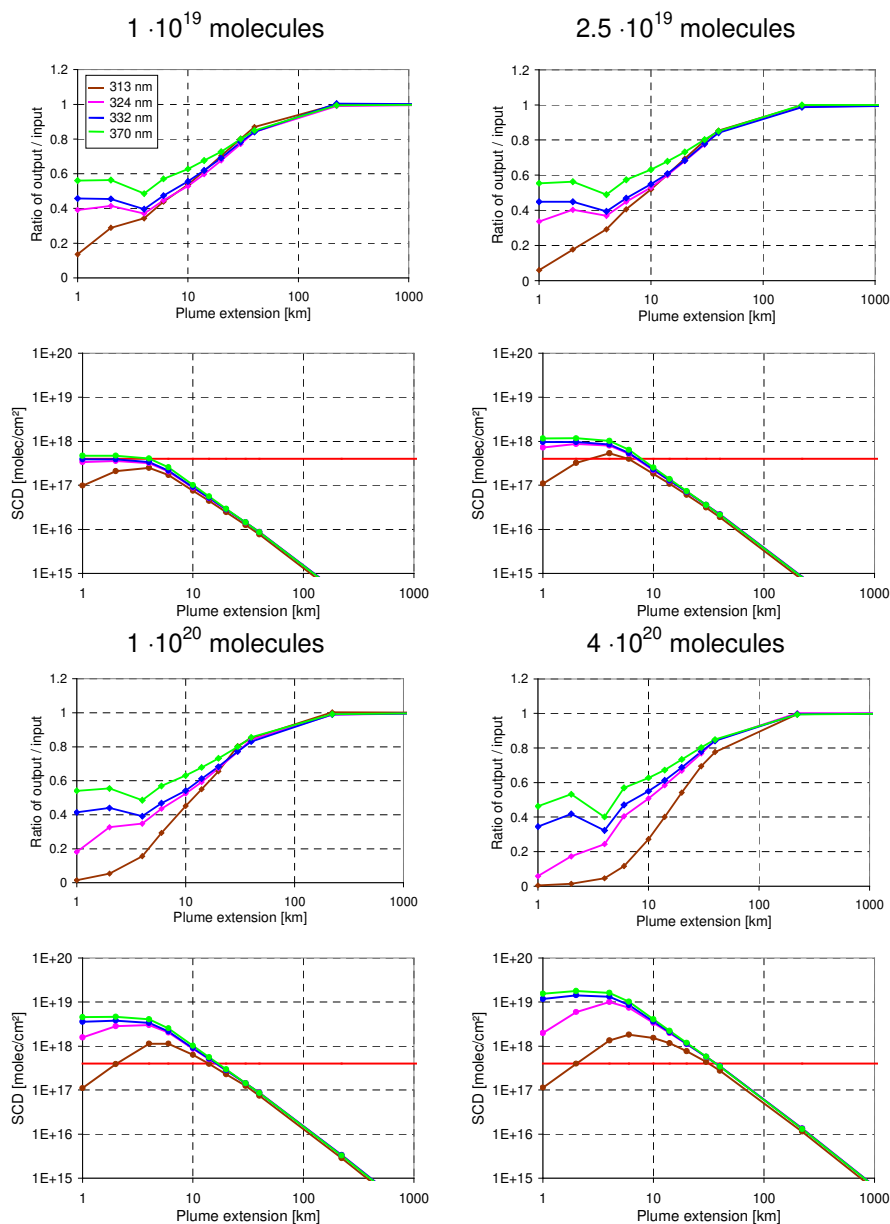
Fig. 14 Derived fraction of the plume molecules (top) and SO₂ SCDs from TROPOMI measurements at different wavelengths as function of the plume size and for different amounts of molecules in the plume. The red horzizontal line indicates the threshold, above which the operational SO₂ retrieval switches from the standard fit window to the first alternative fit window (at longer wavelengths).

1140

1145
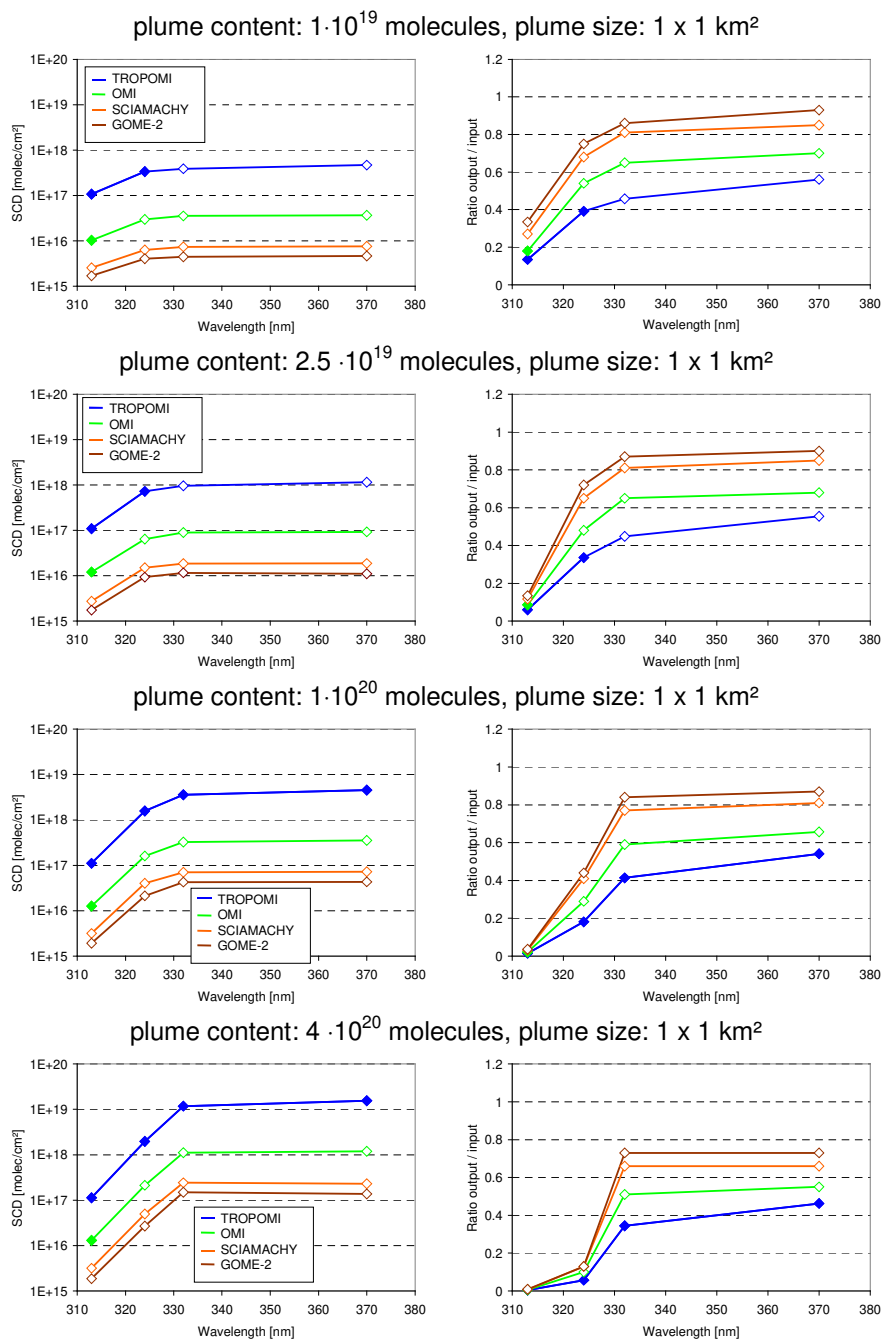
Fig. 15 Fractions (output / input amount of the SO₂ plume) and SO₂ SCDs for different satellite instruments and for

1150 **plume size of 1 x 1 km² as function of the wavelength. The full symbols represent measurements with SCDs above the**

detection limit.

1155
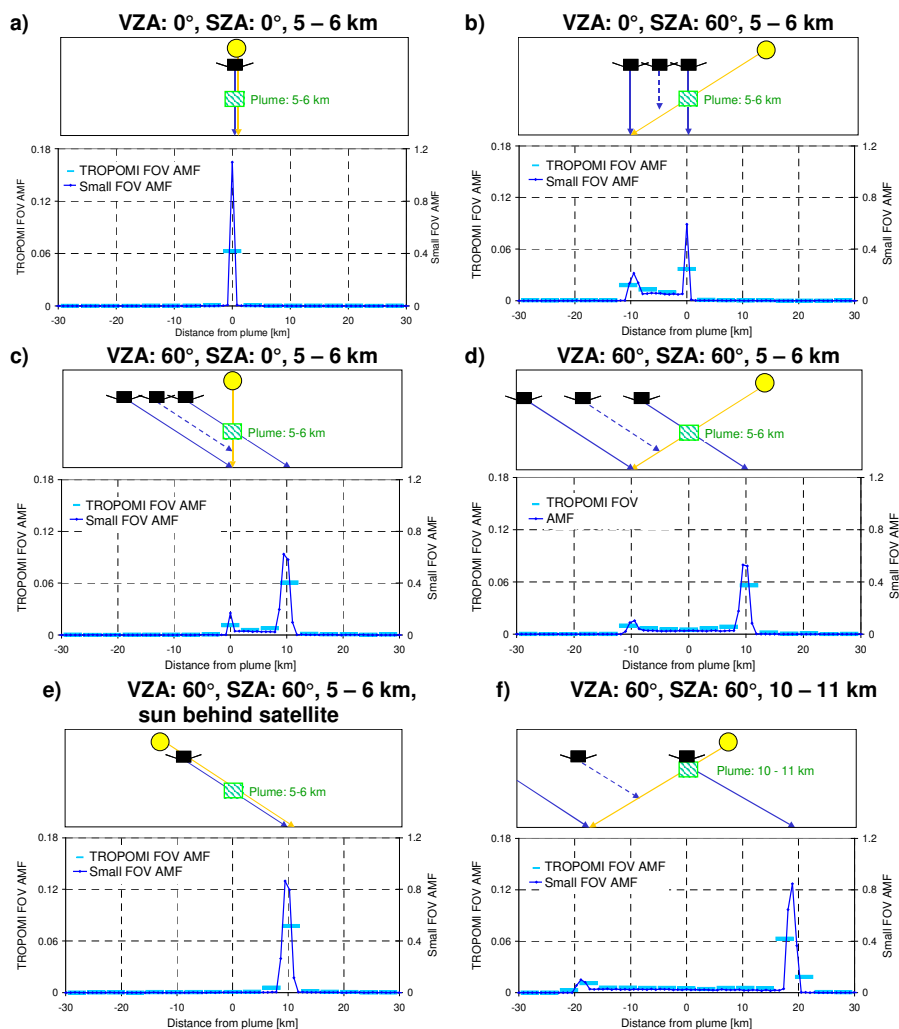
Fig. 16 AMFs for TROPOMI observations of elevated plumes for different combinations of SZA and VZA. The blue lines show the AMFs for observations with a narrow FOV (~ 0.014°) (right y axis); the bright blue symbols represent simulations with a TROPOMI FOV (left axis). All simulations are for 440 nm and plume sizes of 1 x 1 x 1 km³.

1160

1165

1170
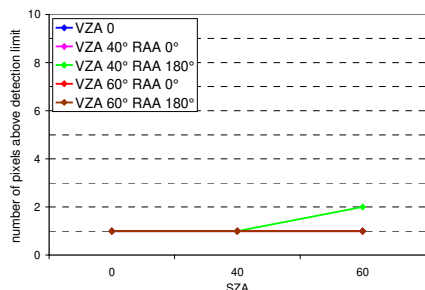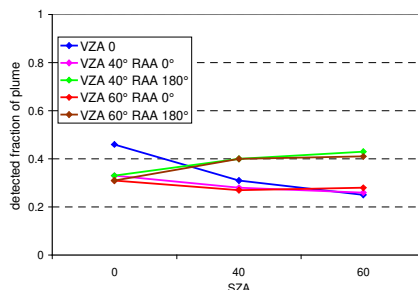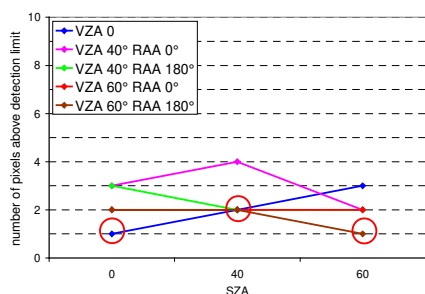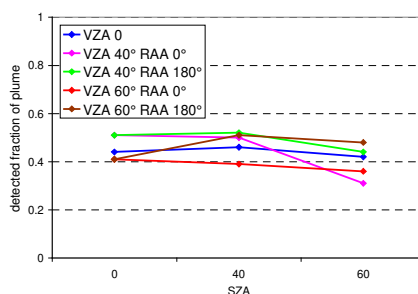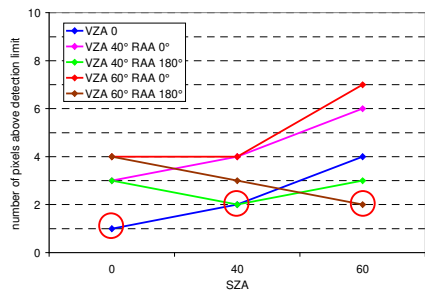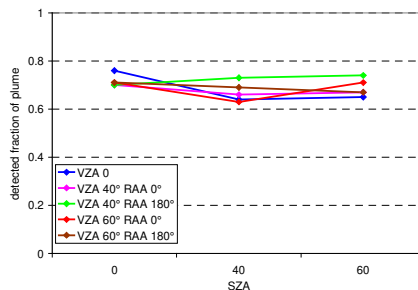
Fig. 17 Number of satellite pixels with SCD above the detection limit (left) and detected fraction of the plume amount (right) for TROPOMI observations with different viewing and solar zenith angles. The plume has an extension of 1 x 1 x 1 km³ and is located at 5 – 6 km altitude. Left: results for the scenario IO VCD$_{low}$; right: results for scenario IO VCD$_{high}$ (see table 3). The red circles indicate scenarios with the sun and the satellite in the same direction for which
1175   **the smearing effect is smallest. RAA indicates the relative azimuth angle between the viewing direction and the sun. Here a RAA of 180° represents cases where the sun shines in the same direction of the satellite view.**

1180

a) 440 nm

Atmospheric
Measurement
Techniques
Discussions

1210

b) 313 nm

VZA: 60, SZA: -50   VZA: 60, SZA: 0   VZA: 60, SZA: 50
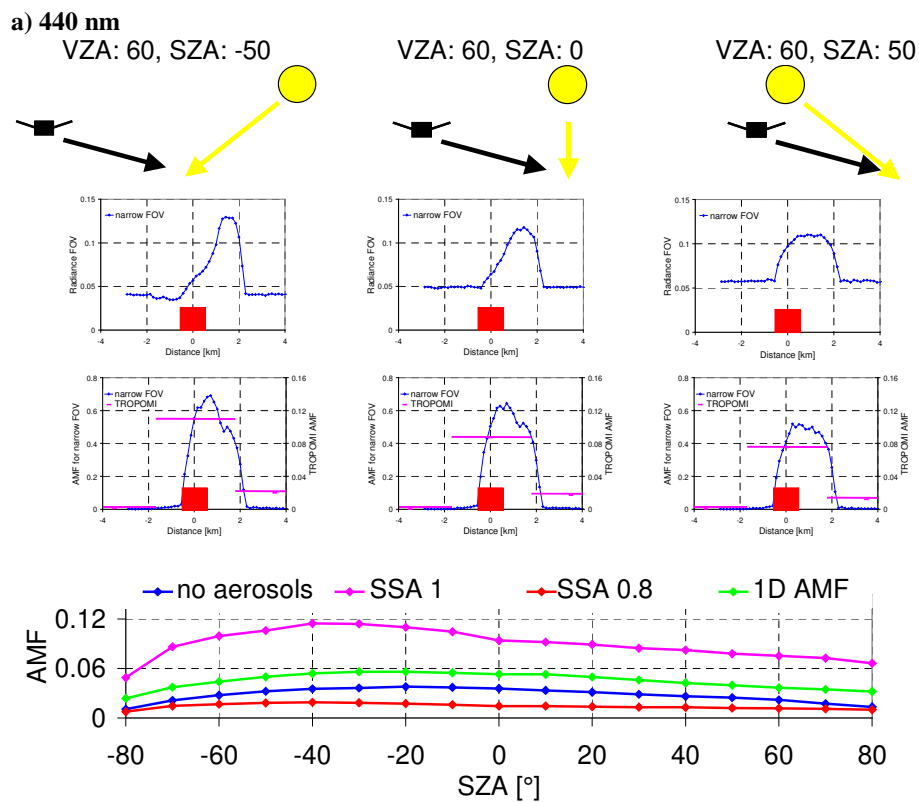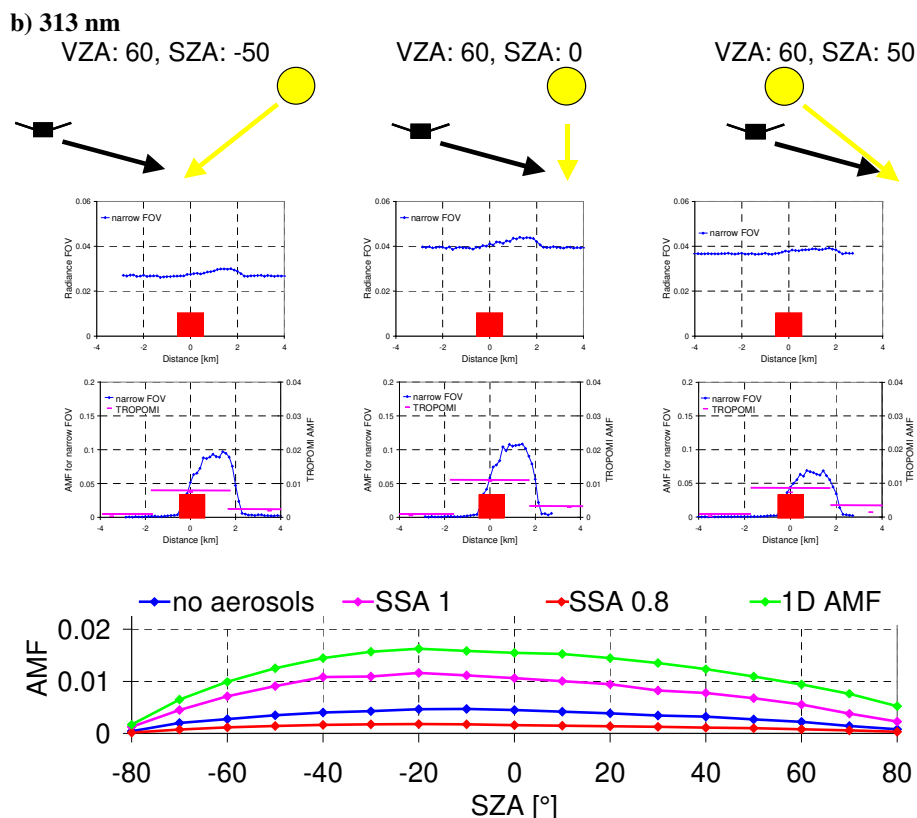
Fig. 18 Dependence of the AMF and normalised radiance for a slant viewing angle (VZA = 60°) on the illumination angle for 440 nm (a) and 313 nm (b). The upper panels show sketches of the investigated viewing and illumination angles (SZA of -50°, 0°, 50°). The middle panels show the normalised radiances and AMFs for these scenarios (for plumes with scattering aerosols) as function of the relative distance from the plume (1 x 1 x 1 km³, red boxes). Note the different y-axes for the AMFs calculated for a narrow FOV (left) or TROPOMI FOV (right). The plume is located directly above the surface (0 – 1 km). The bottom panels show the AMFs for a TROPOMI FOV as function of the SZA. The different lines represent 3D-AMFs for plumes without aerosols (blue), with scattering (magenta) and absorbing (red) aerosols as well as the 1D-AMF (without aerosols).
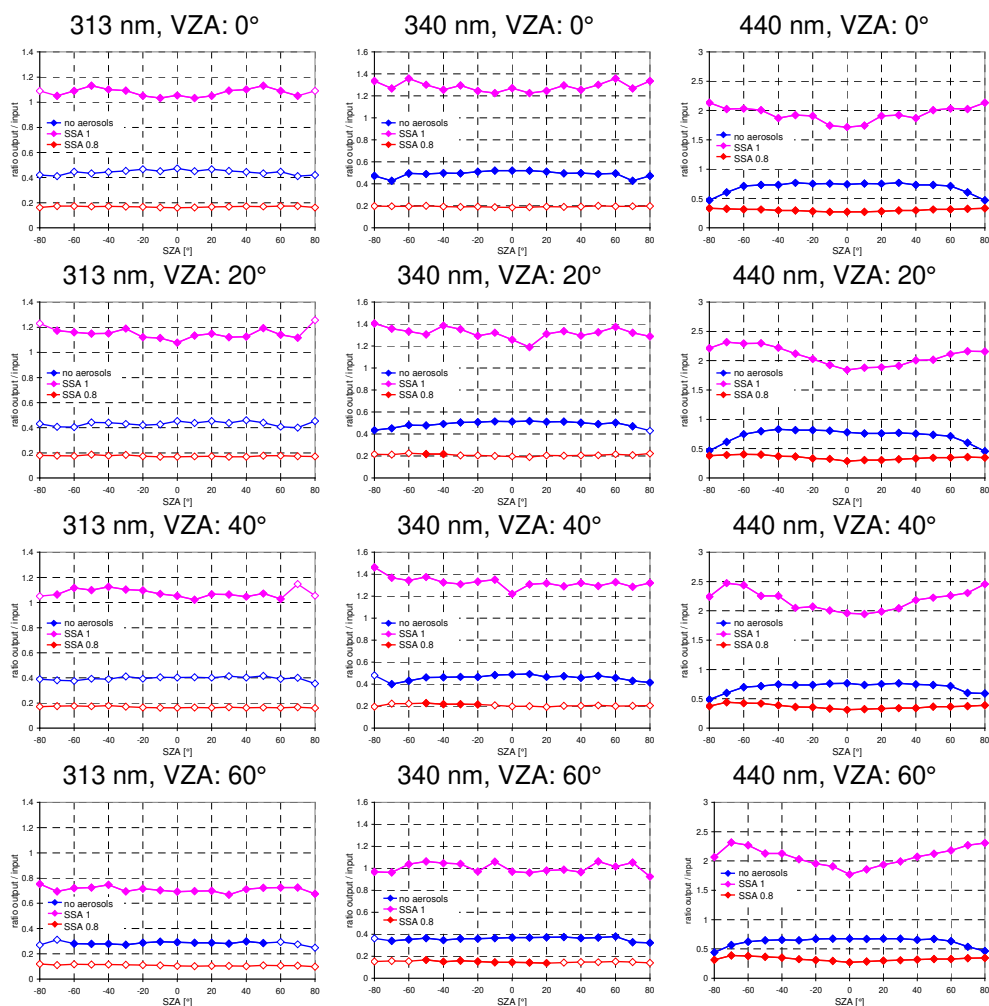
1220

1225

1230

37

1235

Fig. 19 Ratios of the 3D-AMFs for 313 nm (left), 340 nm (center) and 440 nm (right) divided by the corresponding 1D-AMFs as function of the SZA for different viewing angles (blue: plume without aerosols; magenta: plume with scattering aerosols; red: plume with absorbing aerosols). Symbols in full colour represent results above the detection limit.
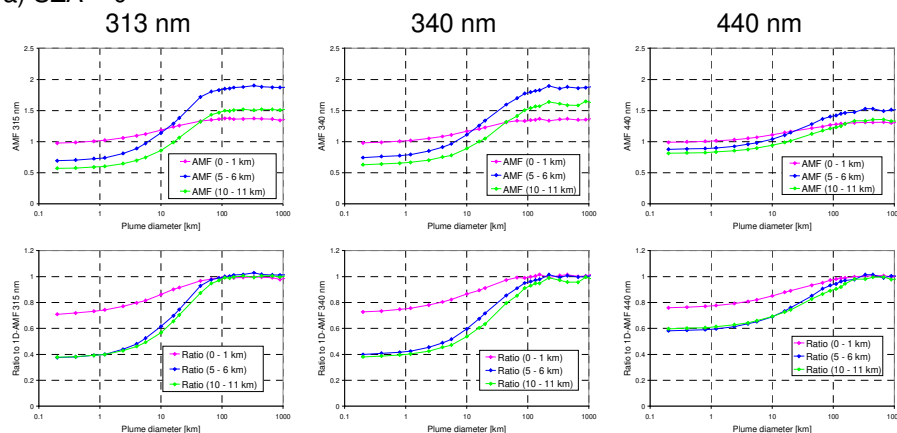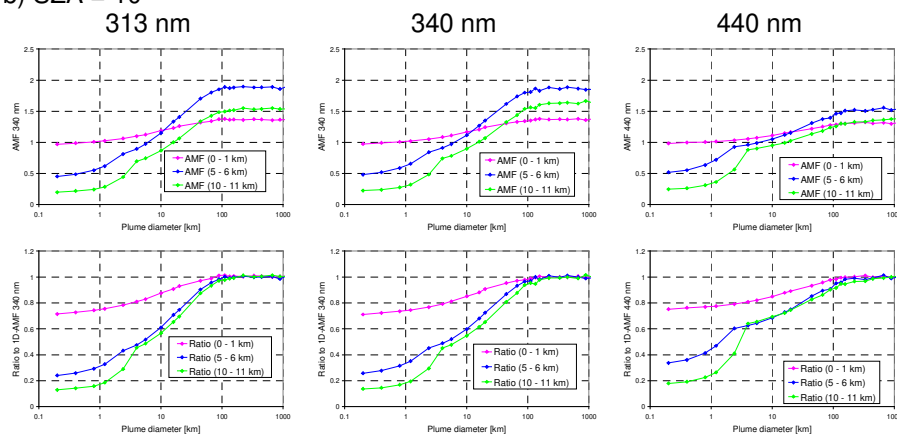
1240

1245

1250

Atmospheric
Measurement
Techniques
Discussions

a) SZA = 0°

b) SZA = 10°

Fig. 20 Dependence of the AMF on the horizontal plume extension for ground based observations (FOV: 0.014°, VZA = 0°, SZA = 0 (a) and SZA = 10° (b). In the upper panels the AMFs for different plume altitudes and wavelengths are shown. In the bottom panels the AMFs normalised by the corresponding 1D AMFs are shown.

Appendix A1 Differential absorption cross sections for the selected trace gases and wavelengths

The following table shows a summary of the differential absorption cross sections used in this study to relate the trace gas SCDs to the corresponding optical depths.

1285 The values were determined by convolution of the original cross section with a Gaussion slit function with FWHM of 0.5 nm (similar to TROPOMI). In addition to the IO absorption cross section also those of H_2O and NO_2 are shown, which could also be analysed in the same spectral range around 440 nm. Note that the absorption cross sections depend on temperature. Also the values from different studies differ, especially for IO and H_2O. Finally, the differential absorption cross sections will depend on the spectral resolution of the instrument. Thus the values in Table A.1.1 can serve as useful reference (e.g. in

1290 this study), but might differ for other applications.

Table A1.1 Differential absorption cross sections for the trace gases considered in this study.

Trace gas, wavelength	Differential absorption cross section after convolution
SO_2, 313 nm (Bogumil et al., 2000)	$1 \cdot 10^{-19}$ cm²
SO_2, 324 nm (Bogumil et al., 2000)	$4 \cdot 10^{-21}$ cm²
SO_2, 332 nm (Bogumil et al., 2000)	$4 \cdot 10^{-22}$ cm²
SO_2, 370 nm (Bogumil et al., 2000)	$5 \cdot 10^{-22}$ cm²
BrO, 340 nm (Wilmouth et al., 1999)	$1.7 \cdot 10^{-17}$ cm²
IO, 440 nm (Hönninger, 2000)	$2 \cdot 10^{-17}$ cm²
NO_2, 440 nm (Vandaele et al., 1997)	$3 \cdot 10^{-19}$ cm²
H_2O, 440 nm (Rothman et al., 2005)	$3.4 \cdot 10^{26}$ cm²

1295 **Appendix A2 Effect of the wavelength dependence of the AMF**

In this section we quantify the effect of the wavelength dependence of the AMF for selected representative scenarios by the comparison of the results of two simulations:

a) monochromatic AMFs (only affected by the saturation effect)

1300 b) ‚true' AMFs (affected by the saturation effect and the wavelength dependence of the AMF)

The ‚true' AMFs are calculated in the following way (see also Marquard et al., 2000): first a measured spectrum for a selected SO_2 scenario is simulated at 'high' spectral resolution (~0.22 FWHM, the spectral resolution of the SO_2 cross section). In order to minimise the computational effort for Monte Carlo simulations (and also to minimise the noise), the spectra are calculated in the following way: first a wavelength close to the center of a SO_2 fit range is chosen. For this

1305 wavelength, the radiance is simulated as function of the absorption cross section. Note that in order to minimise the noise the same photon trajectories are used for the simulations with different absorption cross sections. Based on the derived relationship between the radiance and the absorption cross section, a high resolution spectrum for the selected SO_2 scenario is calculated and convolved by the instrument slit function (here we assume a FWHM of 0.5 nm). In the next step, the simulated spectra are analysed by DOAS similar to the measured spectra. Finally, the derived SO_2 SCD is divided by the

1310 SO_2 VCD (used as input for the respective scenario) to yield the ‚true' AMF.

The upper part of Figure A2.1 shows the ‚true AMFs' derived for the standard fit window around 313 nm and the corresponding monochromatic AMFs for single wavelengths for 4 different plume scenarios. Additional results for 332 nm are shown in the bottom part of the figure. Besides the AMFs, also the ratios of the monochromatic AMFs and the true AMFs are shown. For scenarios with high AMFs (monochromatic AMFs > about 0.6), the difference between the

1315 monochromatic AMFs and the true AMFs is small (<10%), but for smaller AMFs, the difference increases (up to more than 50% for monochromatic AMF below about 0.4). In Fig. A2.2, the ratios of the true AMFs and monochromatic AMFs as function of the vertical optical depth of the SO_2 absorption are shown. For the same fit window, a similar dependence is
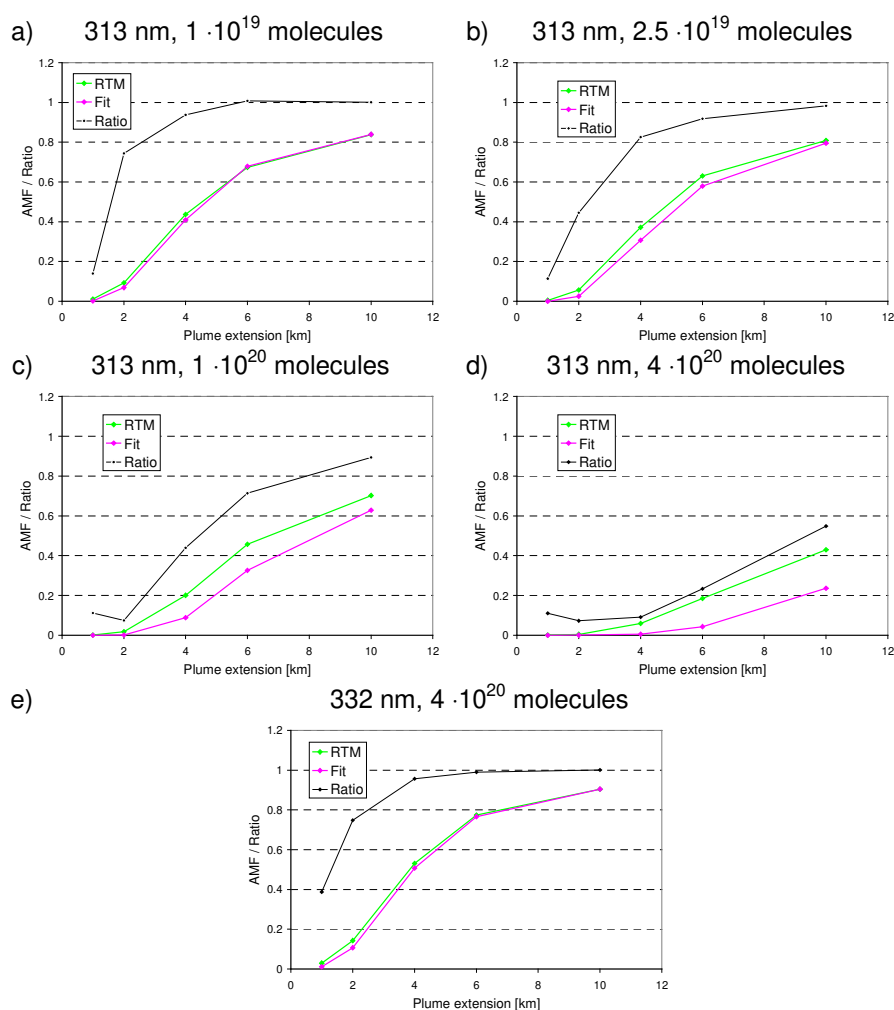
found, almost independent from the SO_2 scenario. However, a different relationship is found for a different fit window indicating the specific spectral patterns of the SO_2 absorption in the different fit windows.

1320 These findings indicate that for an accurate quantitative assessment, true AMFs for selected plume scenarios and wavelengths have to be individually calculated. Nevertheless, for the wavelengths considered here, the underestimation is < 5% if the vertical OD is below about 2.5%.

It should be also noted that for scenarios with high optical depth, the 'optical definition' of the AMF (equation 1) should be used for the interpretation of the measurements. For such cases, the AMFs calculated based on geometric photon trajectories

1325 (e.g. box-AMFs) will differ from those calculated by equation 1 in Pukite and Wagner (2016).

a) 313 nm, $1 \cdot 10^{19}$ molecules   b) 313 nm, $2.5 \cdot 10^{19}$ molecules

c) 313 nm, $1 \cdot 10^{20}$ molecules   d) 313 nm, $4 \cdot 10^{20}$ molecules

e) 332 nm, $4 \cdot 10^{20}$ molecules

Fig. A2.1 True AMFs (magenta lines) and monochromatic AMFs (green lines) as function of the horizontal plume extension for different SO_2 scenarios. Also the ratios of both AMFs are shown (black lines). The AMFs and AMF ratios depend on the wavelength and the SO_2 amount.

1330
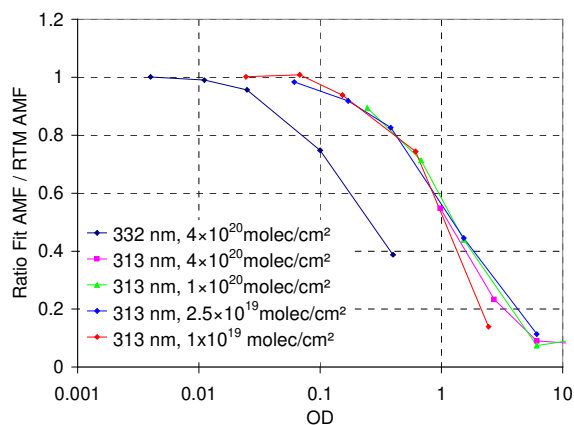
1335

Fig. A2.2 Ratio between true AMFs and monochromatic AMFs as function of the vertical optical depth of SO$_2$ in the plume.
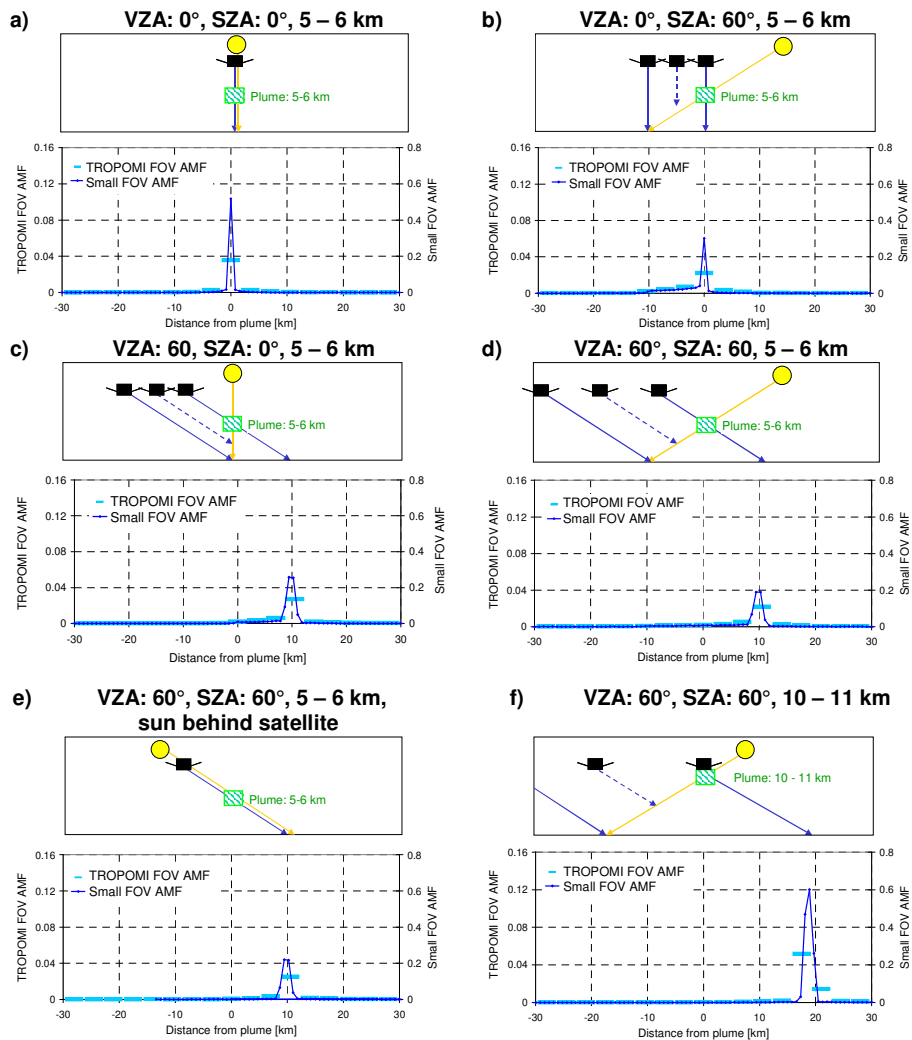
1340

1345

1350

1355

1360

1365

1370

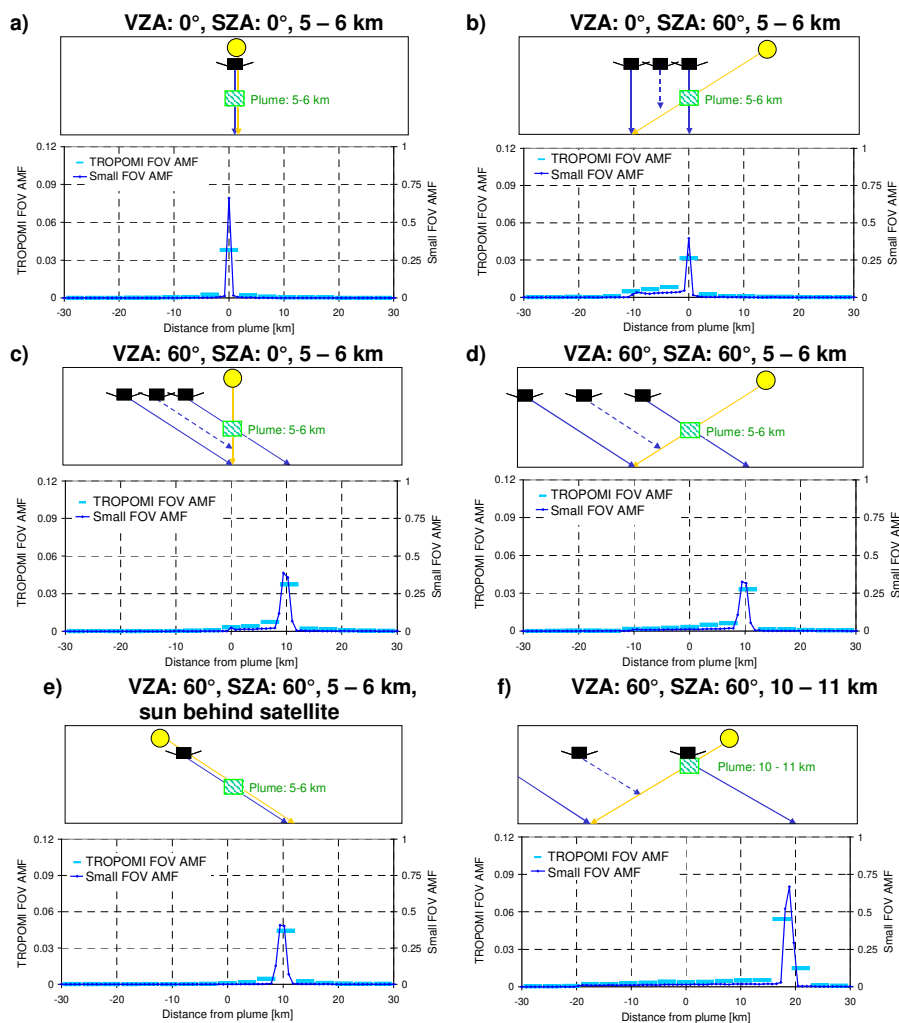**Appendix A3 Geometric effects for 313 nd 340 nm**

1375

Fig. A3.1 AMFs for TROPOMI observations of elevated plumes for different combinations of SZA and VZA. The blue lines show the AMFs for observations with a narrow FOV (~0.014°) (right y axis); the bright blue symbols represent simulations with a TROPOMI FOV (left axis). All simulations are for 313 nm and plume sizes of 1 x 1 x 1 km³.

1380

1385

1390

Atmospheric
Measurement
Techniques

Open Access

Discussions

EGU

Fig. A3.2 AMFs for TROPOMI observations of elevated plumes for different combinations of SZA and VZA. The blue lines show the AMFs for observations with a narrow FOV (~ 0.014°) (right y axis); the bright blue symbols represent simulations with a TROPOMI FOV (left axis). All simulations are for 340 nm and plume sizes of 1 x 1 x 1 km³.